

1 A search for sparticles in zero lepton final states

2 Russell W. Smith

3 Submitted in partial fulfillment of the

4 requirements for the degree of

5 Doctor of Philosophy

6 in the Graduate School of Arts and Sciences

7 COLUMBIA UNIVERSITY

8 2016

9

© 2016

10

Russell W. Smith

11

All rights reserved

12

ABSTRACT

13

A search for sparticles in zero lepton final states

14

Russell W. Smith

15 TODO : Here's where your abstract will eventually go. The above text is all in the
16 center, but the abstract itself should be written as a regular paragraph on the page,
17 and it should not have indentation. Just replace this text.

Contents

19	Contents	i
20	1 Introduction	1
21	2 The Standard Model	5
22	2.1 Overview	5
23	2.2 Field Content	5
24	2.3 Deficiencies of the Standard Model	15
25	3 Supersymmetry	21
26	3.1 Supersymmetric theories : from space to superspace	21
27	3.2 Minimally Supersymmetric Standard Model	24
28	3.3 Phenomenology	30
29	3.4 How SUSY solves the problems with the SM	33
30	3.5 Conclusions	35
31	4 The Large Hadron Collider	37
32	4.1 Basics of Accelerator Physics	37
33	4.2 Accelerator Complex	39
34	4.3 Large Hadron Collider	41
35	4.4 Dataset Delivered by the LHC	43
36	5 The ATLAS detector	49

37	5.1	Magnets	50
38	5.2	Inner Detector	52
39	5.3	Calorimetry	56
40	5.4	Muon Spectrometer	61
41	5.5	Trigger System	66
42	6	Physics Object Reconstruction	73
43	6.1	Primitive Object Reconstruction	73
44	6.2	Physics Object Reconstruction	73
45	7	The Recursive Jigsaw Technique	75
46	7.1	Razor variables	75
47	7.2	SuperRazor variables	75
48	7.3	The Recursive Jigsaw Technique	75
49	7.4	Variables used in the search for zero lepton SUSY	75
50	8	Table of Contents Title	77
51	9	A search for supersymmetric particles in zero lepton final states with the Recursive Jigsaw Technique	79
53	9.1	Object reconstruction	79
54	9.2	Signal regions	80
55	9.3	Background estimation	80
56	10	Results	81
57	10.1	Statistical Analysis	81
58	10.2	Signal Region distributions	81
59	10.3	Pull Plots	81
60	10.4	Systematic Uncertainties	81
61	10.5	Exclusion plots	81

62	Conclusion	83
63	10.6 New Section	83
64	Bibliography	85
65	Quantum Field Theory and Symmetries	93
66	Quantum Field Theory	93
67	Symmetries	94
68	Local symmetries	96

Acknowledgements

Dedication

71

Chapter 1

72

Introduction

73 Particle physics is a remarkably successful field of scientific inquiry. The ability to
 74 precisely predict the properties of a exceedingly wide range of physical phenomena,
 75 such as the description of the cosmic microwave background [1, 2], the understanding
 76 of the anomalous magnetic dipole moment of the electron [3, 4], and the measurement
 77 of the number of weakly-interacting neutrino flavors [5] is truly amazing.

78 The theory that has allowed this range of predictions is the *Standard Model*
 79 of particle physics (SM). The Standard Model combines the electroweak theory of
 80 Glashow, Weinberg, and Salam [6–8] with the theory of the strong interactions, as
 81 first envisioned by Gell-Mann and Zweig [9, 10]. This quantum field theory (QFT)
 82 contains a tiny number of particles, whose interactions describe phenomena up to at
 83 least the TeV scale. These particles are manifestations of the fields of the Standard
 84 Model, after application of the Higgs Mechanism. The particle content of the SM
 85 consists only of the six quarks, the six leptons, the four gauge bosons, and the scalar
 86 Higgs boson.

87 Despite its impressive range of described phenomena, the Standard Model has
 88 some theoretical and experimental deficiencies. The SM contains 26 free parameters
 89 ¹. It would be more theoretically pleasing to understand these free parameters in
 90 terms of a more fundamental theory. The major theoretical concern of the Standard
 91 Model, as it pertains to this thesis, is the *hierarchy problem*[11–15]. The light mass

¹This is the Standard Model corrected to include neutrino masses. These parameters are the fermion masses (6 leptons, 6 quarks), CKM and PMNS mixing angles (8 angles, 2 CP-violating phases), W/Z/Higgs masses (3), the Higgs field expectation value, and the couplings of the strong, weak, and electromagnetic forces (3 α_{force}).

of the Higgs boson (125 GeV) should be quadratically dependent on the scale of UV physics, due to the quantum corrections from high-energy physics processes. The most perplexing experimental issue is the existence of *dark matter*, as demonstrated by galactic rotation curves [16–22]. This data has shown that there exists additional matter which has not yet been seen interacting with the particles of the Standard Model. There is no particle in the SM which can act as a candidate for dark matter.

Both of these major issues, as well as numerous others, can be solved by the introduction of *supersymmetry* (SUSY) [15, 23–35]. In supersymmetric theories, each SM particles has a so-called *superpartner*, or sparticle partner, differing from given SM particle by 1/2 in spin. These theories solve the hierarchy problem, since the quantum corrections induced from the superpartners exactly cancel those induced by the SM particles. In addition, these theories are usually constructed assuming *R*–parity, which can be thought of as the “charge” of supersymmetry, with SM particles having $R = 1$ and sparticles having $R = -1$. In collider experiments, since the incoming SM particles have total $R = 1$, the resulting sparticles are produced in pairs. This produces a rich phenomenology, which is characterized by significant hadronic activity and large missing transverse energy (E_T^{miss}), which provide significant discrimination against SM backgrounds [36].

Despite the power of searches for supersymmetry where E_T^{miss} is a primary discriminating variable, there has been significant interest in the use of other variables to discriminate against SM backgrounds. These include searches employing variables such as αT , $M_{T,2}$, and the razor variables (M_R, R^2) [37–47]. In this thesis, we will present the first search for supersymmetry using the novel Recursive Jigsaw Reconstruction (RJR) technique. RJR can be considered the conceptual successor of the razor variables. We impose a particular final state “decay tree” on an events, which roughly corresponds to a simplified Feynmann diagram in decays containing weakly-interacting particles. We account for the missing degrees of freedom associated

119 to the weakly-interacting particles by a series of simplifying assumptions, which allow
120 us to calculate our variables of interest at each step in the decay tree. This allows an
121 unprecedented understanding of the internal structure of the decay and the ability to
122 construct additional variables to reject Standard Model backgrounds.

123 This thesis details a search for the superpartners of the gluon and quarks, the
124 gluino and squarks, in final states with zero leptons, with 13.3 fb^{-1} of data using the
125 ATLAS detector. We organize the thesis as follows. The theoretical foundations of
126 the Standard Model and supersymmetry are described in Chapters 2 and 3. The
127 Large Hadron Collider and the ATLAS detector are presented in Chapters 4 and 5.
128 Chapter 5 provides a detailed description of Recursive Jigsaw Reconstruction and a
129 description of the variables used for the particular search presented in this thesis.
130 Chapter 6 presents the details of the analysis, including details of the dataset, object
131 reconstruction, and selections used. In Chapter 7, the final results are presented;
132 since there is no evidence of a supersymmetric signal in the analysis, we present the
133 final exclusion curves in simplified supersymmetric models.

136 **2.1 Overview**

137 A Standard Model is another name for a theory of the internal symmetry group
 138 $SU(3)_C \otimes SU(2)_L \otimes U(1)_Y$, with its associated set of parameters. *The Standard*
 139 Model refers specifically to a Standard Model with the proper parameters to describe
 140 the universe. The SM is the culmination of years of work in both theoretical
 141 and experimental particle physics. In this thesis, we take the view that theorists cite

142 construct a model with the field content and symmetries as inputs, and write down the
 143 most general Lagrangian consistent with those symmetries. Assuming this model is
 144 compatible with nature (in particular, the predictions of the model are consistent with
 145 previous experiments), experimentalists are responsible measuring the parameters of
 146 this model. This will be applicable for this chapter and the following one.

147 Additional theoretical background is in 10.6. The philosophy and notations are
 148 inspired by [48, 49].

149 **2.2 Field Content**

The Standard Model field content is

$$\begin{aligned} \text{Fermions} &: Q_L(3, 2)_{+1/3}, U_R(3, 1)_{+4/3}, D_R(3, 1)_{-2/3}, L_L(1, 2)_{-1}, E_R(1, 1)_{-2} \\ \text{Scalar (Higgs)} &: \phi(1, 2)_{+1} \\ \text{Vector Fields} &: G^\mu(8, 1)_0, W^\mu(1, 3)_0, B^\mu(1, 1)_0 \end{aligned} \tag{2.1}$$

150 where the $(A, B)_Y$ notation represents the irreducible representation under $SU(3)$
151 and $SU(2)$, with Y being the electroweak hypercharge. Each of these fermion fields
152 has an additional index, representing the three generation of fermions.

153 We observed that Q_L, U_R , and D_R are triplets under $SU(3)_C$; these are the *quark*
154 fields. The *color* group, $SU(3)_C$ is mediated by the *gluon* field $G^\mu(8, 1)_0$, which has
155 8 degrees of freedom. The fermion fields $L_L(1, 2)_{-1}$ and $E_R(1, 1)_{-2}$ are singlets under
156 $SU(3)_C$; we call them the *lepton* fields.

157 Next, we note the “left-handed” (“right-handed”) fermion fields, denoted by L (R)
158 subscript, The left-handed fields form doublets under $SU(2)_L$. These are mediated
159 by the three degrees of freedom of the “W” fields $W^\mu(1, 3)_0$. These fields only act
160 on the left-handed particles of the Standard Model. This is the reflection of the
161 “chirality” of the Standard Model; the left-handed and right-handed particles are
162 treated differently by the electroweak forces. The right-handed fields, U_R, D_R , and
163 E_R , are singlets under $SU(2)_L$.

164 The $U(1)_Y$ symmetry is associated to the $B^\mu(1, 1)_0$ boson with one degree of
165 freedom. The charge Y is known as the electroweak hypercharge.

166 To better understand the phenomenology of the Standard Model, let us investigate
167 each of the *sectors* of the Standard Model separately.

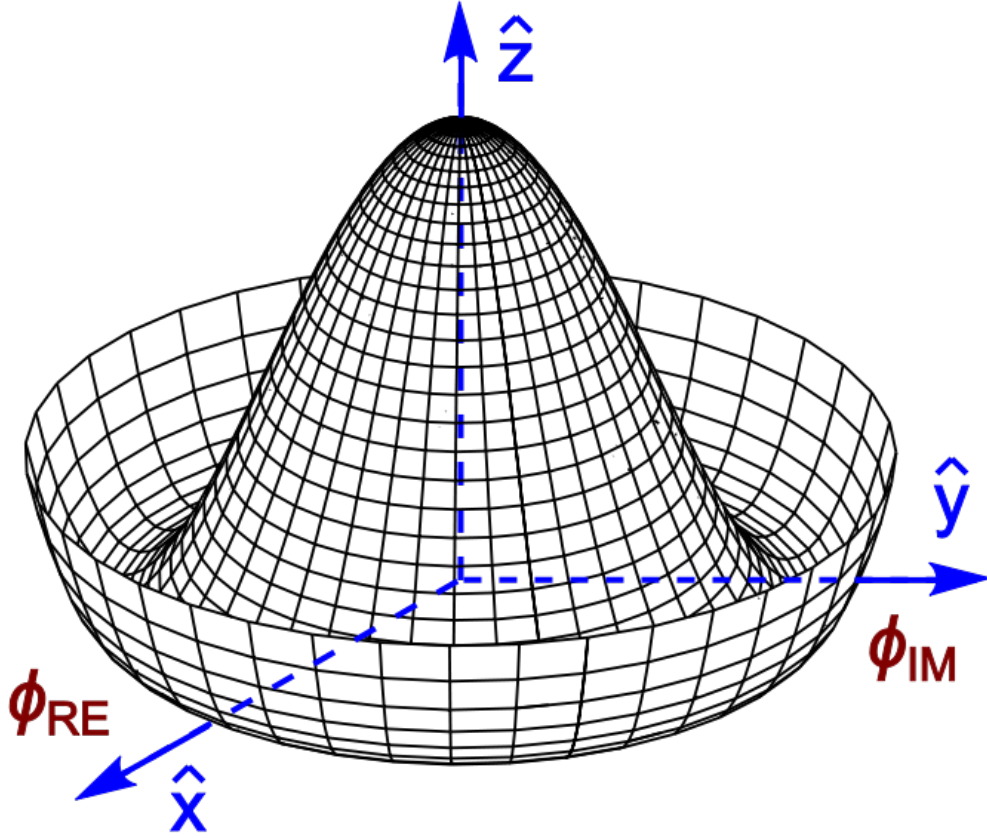
168 Electroweak sector

The electroweak sector refers to the $SU(2)_L \otimes U(1)_Y$ portion of the Standard
Model gauge group. Following our philosophy of writing all gauge-invariant and
renormalizable terms, the electroweak Lagrangian can be written as

$$\mathcal{L} = W_a^{\mu\nu} W_{\mu\nu}^a + B^{\mu\nu} B_{\mu\nu} + (D^\mu \phi)^\dagger D_\mu \phi - \mu^2 \phi^\dagger \phi - \lambda (\phi^\dagger \phi)^2. \quad (2.2)$$

where $W_a^{\mu\nu}$ are the three ($a = 1, 2, 3$) gauge bosons associated to the $SU(2)_L$ gauge
group, $B^{\mu\nu}$ is the one gauge boson of the $U(1)_Y$ gauge group, and ϕ is the complex

Figure 2.1: Sombrero potential



Higgs multiplet. The covariant derivative D^μ is given by

$$D^\mu = \partial^\mu + \frac{ig}{2} W_a^\mu \sigma_a + \frac{ig'}{2} B^\mu \quad (2.3)$$

where $i\sigma_a$ are the Pauli matrices times the imaginary constant, which are the generators for $SU(2)_L$, and g and g' are the $SU(2)_L$ and $U(1)_Y$ coupling constants, respectively. The field strength tensors $W_a^{\mu\nu}$ and $B^{\mu\nu}$ are given by the commutator of the covariant derivative associated to each field

$$B^{\mu\nu} = \partial^\mu B^\nu - \partial^\nu B^\mu \quad (2.4)$$

$$W_a^{\mu\nu} = \partial^\mu W_a^\nu - \partial^\nu W_a^\mu - g\epsilon_{abc} W_a^\mu W_b^\nu, \quad i = 1, 2, 3$$

170 The terms in the Lagrangian 2.2 proportional to μ^2 and λ make up the “Higgs
 171 potential” [50]. As normal (see Appendix 10.6), we restrict $\lambda > 0$ to guarantee our
 172 potential is bounded from below, and we also require $\mu^2 < 0$, which gives us the
 173 standard “sombrero” potential shown in 2.1.

This potential has infinitely many minima at $\langle \phi \rangle = \sqrt{2m/\lambda}$; the ground state is *spontaneously* broken by the choice of ground state, which induces a vacuum expectation value (VEV). Without loss of generality, we can choose the Higgs field ϕ to point in the real direction, and write the Higgs field ϕ in the following form :

$$\phi = \frac{1}{\sqrt{2}} \exp\left(\frac{i}{v} \sigma_a \theta_a\right) \begin{pmatrix} 0 \\ v + h(x) \end{pmatrix}. \quad (2.5)$$

We choose a gauge to rotate away the dependence on θ_a , such that we can write simply

$$\phi = \frac{1}{\sqrt{2}} \begin{pmatrix} 0 \\ v + h(x) \end{pmatrix}. \quad (2.6)$$

Now, we can see how the masses of the vector bosons are generated from the application of the Higgs mechanism. We plug Eq.2.6 back into the electroweak Lagrangian, and only showing the relevant mass terms in the vacuum state where $h(x) = 0$ see that (dropping the Lorentz indices) :

$$\begin{aligned} \mathcal{L}_M &= \frac{1}{8} \left| \begin{pmatrix} gW_3 + g'B & g(W_1 - iW_2) \\ g(W_1 + iW_2) & -gW_3 + g'B \end{pmatrix} \begin{pmatrix} 0 \\ v \end{pmatrix} \right|^2 \\ &= \frac{g^2 v^2}{8} \left[W_1^2 + W_2^2 + \left(\frac{g'}{g} B - W_3 \right)^2 \right] \end{aligned} \quad (2.7)$$

Defining the Weinberg angle $\tan(\theta_W) = g'/g$ and the following *physical* fields :

$$W^\pm = \frac{1}{\sqrt{2}} (W_1 \mp iW_2) \quad (2.8)$$

$$Z^0 = \cos \theta_W W_3 - \sin \theta_W B$$

$$A^0 = \sin \theta_W W_3 + \cos \theta_W B$$

we can write the piece of the Lagrangian associated to the vector boson masses as

$$\mathcal{L}_{MV} = \frac{1}{4}g^2 v^2 W^+ W^- + \frac{1}{8}(g^2 + g'^2)v^2 Z^0 Z^0. \quad (2.9)$$

and we have the following values of the masses for the vector bosons :

$$\begin{aligned} m_W^2 &= \frac{1}{4}v^2 g^2 \\ m_Z^2 &= \frac{1}{4}v^2(g^2 + g'^2) \\ m_A^2 &= 0 \end{aligned} \quad (2.10)$$

174 We thus see how the Higgs mechanism gives rise to the masses of the W^\pm and Z
175 boson in the Standard Model; the mass of the photon is zero, as expected. The
176 $SU(2)_L \otimes U(1)_Y$ symmetry of the initially massless $W_{1,2,3}$ and B fields is broken to
177 the $U(1)_{EM}$. Of the four degrees of freedom in the complex Higgs doublet, three are
178 “eaten” when we give mass to the W^\pm and Z_0 , while the other degree of freedom is
179 the Higgs particle, as found in 2012 by the ATLAS and CMS collaborations [51, 52].

180 Quantum Chromodynamics

Quantum chromodynamics (or the theory of the *strong* force) characterizes the behavior of *colored* particles, collectively known as *partons*. The partons of the Standard Model are the (fermionic) quarks, and the (bosonic) gluons. The strong force is governed by $SU(3)_C$, an unbroken symmetry in the Standard Model, which implies the gluon remains massless. Defining the covariant derivative for QCD as

$$D^\mu = \partial^\mu + ig_s G_a^\mu L_a, a = 1, \dots, 8 \quad (2.11)$$

where L_a are the generators of $SU(3)_C$, and g_s is the coupling constant of the strong force. The QCD Lagrangian then is given by

$$\mathcal{L}_{QCD} = i\bar{\psi}_f D_\mu \gamma^\mu \psi_f - \frac{1}{4}G_{a,\mu\nu} G_a^{\mu\nu} \quad (2.12)$$

where the summation over f is for quarks *families*, and $G_a^{\mu\nu}$ is the gluon field strength tensor, given by

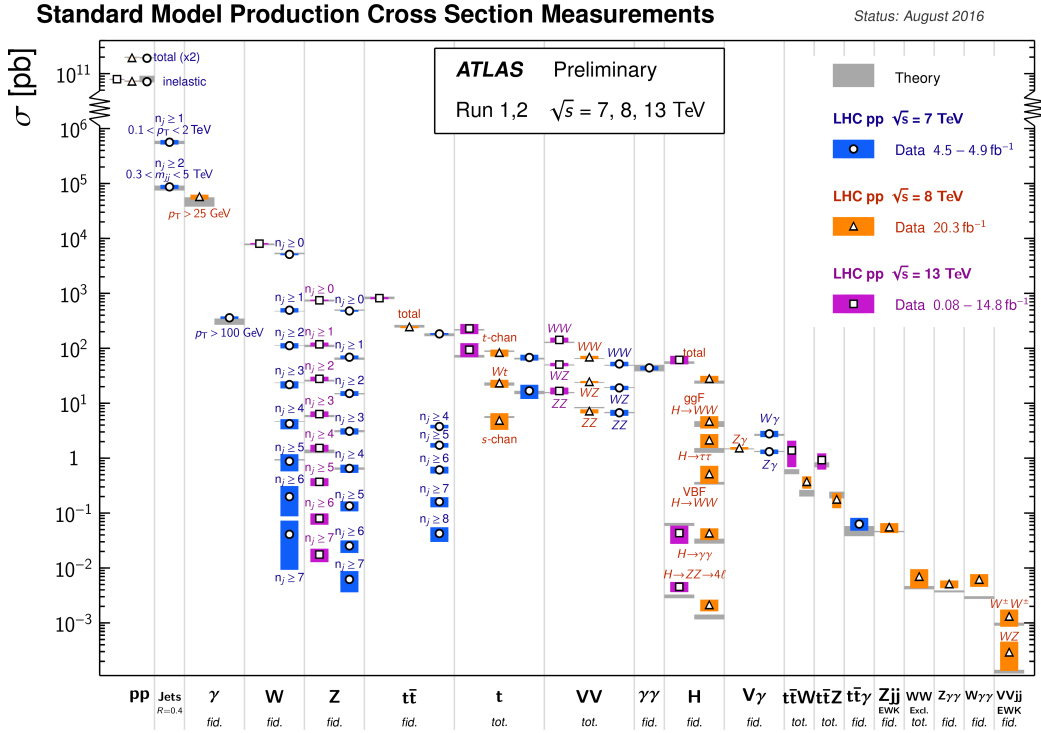
$$G_a^{\mu\nu} = \partial^\mu G_a^\nu - \partial^\nu G_a^\mu - g_s f^{abc} G_b^\mu G_c^\nu, a, b, c = 1, \dots, 8 \quad (2.13)$$

181 where f^{abc} are the structure constants of $SU(3)_C$, which are analogous to ϵ_{abc} for
 182 $SU(2)_L$. The kinetic term for the quarks is contained in the standard ∂_μ term, while
 183 the field strength term contains the interactions between the quarks and gluons, as
 184 well as the gluon self-interactions.

185 Written down in this simple form, the QCD Lagrangian does not seem much
 186 different from the QED Lagrangian, with the proper adjustments for the different
 187 group structures. The gluon is massless, like the photon, so one could naïvely expect
 188 an infinite range force, and it pays to understand why this is not the case. The
 189 reason for this fundamental difference is the gluon self-interactions arising in the
 190 field strength tensor term of the Lagrangian. This leads to the phenomena of *color*
 191 *confinement*, which describes how one only observes color-neutral particles alone in
 192 nature. In contrast to the electromagnetic force, particles which interact via the
 193 strong force experience a *greater* force as the distance between the particles increases.
 194 At long distances, the potential is given by $V(r) = -kr$. At some point, it is more
 195 energetically favorable to create additional partons out of the vacuum than continue
 196 pulling apart the existing partons, and the colored particles undergo *fragmentation*.
 197 This leads to *hadronization*. Bare quarks and gluons are actually observed as sprays
 198 of hadrons (primarily kaons and pions); these sprays are known as *jets*, which are
 199 what are observed by experiments.

200 It is important to recognize the importance of understanding these QCD inter-
 201 actions in high-energy hadron colliders such as the LHC. Since protons are hadrons,
 202 proton-proton collisions such as those produced by the LHC are primarily governed by
 203 the processes of QCD. In particular, by far the most frequent process observed in LHC
 204 experiments is dijet production from gluon-gluon interactions (see Fig.2.2). These

Figure 2.2: Cross-sections of various Standard Model processes



205 gluons that interact are part of the *sea* particles inside the proton; the simple $p = uud$
 206 model does not apply. The main *valence* uud quarks are constantly interacting via
 207 gluons, which can themselves radiate gluons or split into quarks, and so on. A more
 208 useful understanding is given by the colloquially-known *bag* model [53, 54], where the
 209 proton is seen as a “bag” of (in principle) infinitely many partons, each with energy
 210 $E < \sqrt{s} = 6.5$ TeV. One then collides this (proton) bag with another, and views the
 211 products of this very complicated collision, where calculations include many loops in
 212 nonperturbative QCD calculations.

213 Fortunately, we are generally saved by the QCD factorization theorems [55]. This
 214 allows one to understand the hard (i.e. short distance or high energy) $2 \rightarrow 2$ parton
 215 process using the tools of perturbative QCD, while making series of approximations
 216 known as a *parton shower* model to understand the additional corrections from
 217 nonperturbative QCD. We will discuss the reconstruction of jets by experiments in
 218 Ch.5.

219 **Fermions**

220 We will now look more closely at the fermions in the Standard Model [56].

221 As noted earlier in Sec.2.2, the fermions of the Standard Model can be first
 222 distinguished between those that interact via the strong force (quarks) and those
 223 which do not (leptons).

There are six leptons in the Standard Model, which can be placed into three
generations.

$$\begin{pmatrix} e \\ \nu_e \end{pmatrix}, \begin{pmatrix} \mu \\ \nu_\mu \end{pmatrix}, \begin{pmatrix} \tau \\ \nu_\tau \end{pmatrix} \quad (2.14)$$

224 There is the electron (e), muon (μ), and tau (τ), each of which has an associated
 225 neutrino (ν_e, ν_μ, ν_τ). Each of the so-called charged (“electron-like”) leptons has
 226 electromagnetic charge -1 , while the neutrinos all have $q_{EM} = 0$.

227 Often in an experimental context, lepton is used to denote the stable electron
 228 and metastable muon, due to their striking experimental signatures. Taus are often
 229 treated separately, due to their much shorter lifetime of $\tau_\tau \sim 10^{-13}s$; these decay
 230 through hadrons or the other leptons, so often physics analyses at the LHC treat
 231 them as jets or leptons, as will be done in this thesis.

232 As the neutrinos are electrically neutral, nearly massless, and only interact via the
 233 weak force, it is quite difficult to observe them directly. Since LHC experiments rely
 234 overwhelmingly on electromagnetic interactions to observe particles, the presence of
 235 neutrinos is not observed directly. Neutrinos are instead observed by the conservation
 236 of four-momentum in the plane transverse to the proton-proton collisions, known as
 237 *missing transverse energy*.

There are six quarks in the Standard Model : up, down, charm, strange, top, and
 bottom. Quarks are similar organized into three generations :

$$\begin{pmatrix} u \\ d \end{pmatrix}, \begin{pmatrix} c \\ s \end{pmatrix}, \begin{pmatrix} t \\ b \end{pmatrix} \quad (2.15)$$

238 where we speak of “up-like” quarks and “down-like” quarks.

239 Each up-like quark has charge $q_{up} = 2/3$, while the down-like quarks have $q_{down} =$
240 $-1/3$. At the high energies of the LHC, one often makes the distinction between
241 the light quarks (u, d, c, s), the bottom quark, and top quark. In general, due to
242 the hadronization process described above, the light quarks, with masses $m_q < \sim$
243 1.5GeV are indistinguishable by LHC experiments. Their hadronic decay products
244 generally have long lifetimes and they are reconstructed as jets.¹. The bottom quark
245 hadronizes primarily through the B -mesons, which generally travels a short distance
246 before decaying to other hadrons. This allows one to distinguish decays via b -quarks
247 from other jets; this procedure is known as *b-tagging* and will be discussed more in
248 Ch.5. Due to its large mass, the top quark decays before it can hadronize; there
249 are no bound states associated to the top quark. The top is of particular interest at
250 the LHC; it has a striking signature through its most common decay mode $t \rightarrow Wb$.
251 Decays via tops, especially $t\bar{t}$ are frequently an important signal decay mode, or an
252 important background process.

253 **Interactions in the Standard Model**

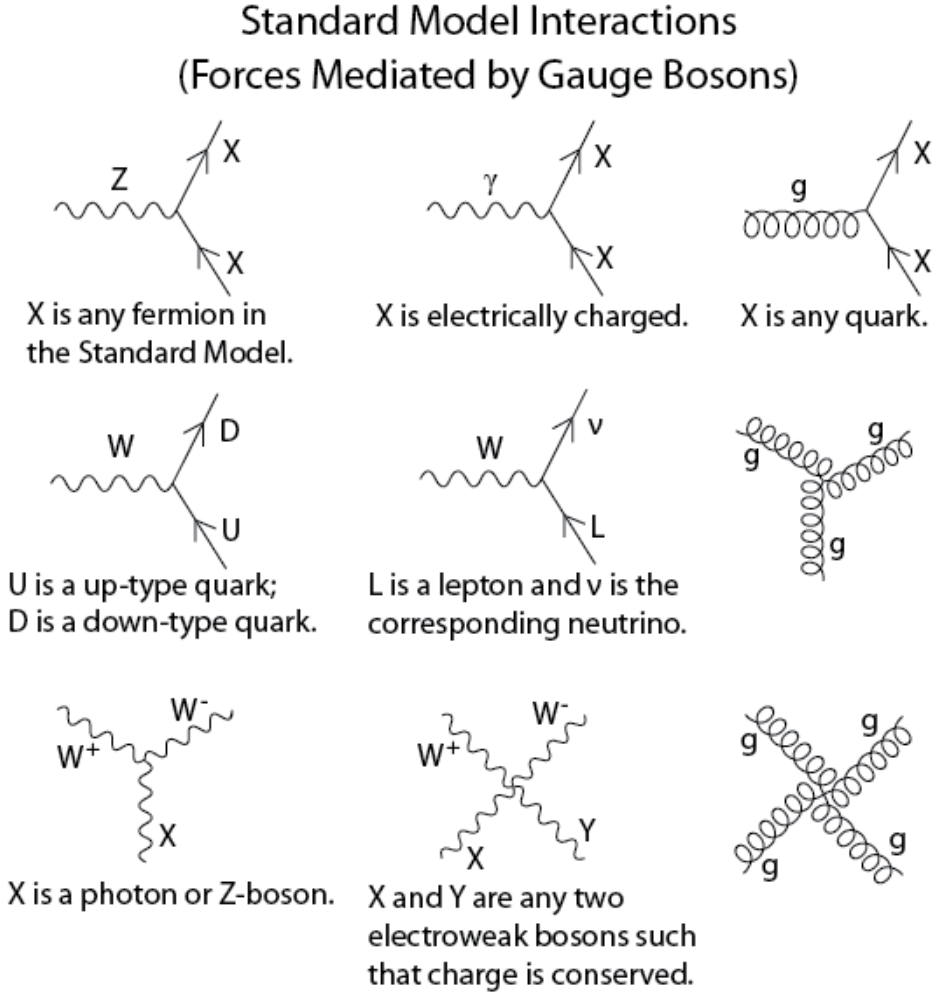
254 We briefly overview the entirety of the fundamental interactions of the Standard
255 Model; these can also be found in 2.3.

256 The electromagnetic force, mediated by the photon, interacts with via a three-
257 point coupling all charged particles in the Standard Model. The photon thus interacts
258 with all the quarks, the charged leptons, and the charged W^\pm bosons.

259 The weak force is mediated by three particles : the W^\pm and the Z^0 . The Z^0 can
260 interacts with all fermions via a three-point coupling. A real Z_0 can thus decay to
261 a fermion-antifermion pair of all SM fermions except the top quark, due to its large

¹In some contexts, charm quarks are also treated as a separate category, although it is quite difficult to distinguish charm quarks from the other light quarks.

Figure 2.3: The interactions of the Standard Model



mass. The W^\pm has two important three-point interactions with fermions. First, the W^\pm can interact with an up-like quark and a down-like quark; an important example in LHC experiments is $t \rightarrow W b$. The coupling constants for these interactions are encoded in the unitary matrix known as the Cabibbo–Kobayashi–Maskawa (CKM) matrix [57, 58], and are generally known as flavor-changing interactions. Secondly, the W^\pm interacts with a charged lepton and its corresponding neutrino. In this case, the unitary matrix that corresponds to CKM matrix for quarks is the identity matrix, which forbids (fundamental) vertices such as $\mu \rightarrow We$. For leptons, instead this is a two-step process : $\mu \rightarrow \nu_m u W \rightarrow \nu_m u \bar{\nu}_e e$. Finally, there are the self-interactions

271 of the weak gauge bosons. There is a three-point and four-point interaction; all
272 combinations are allowed which conserve electric charge.

273 The strong force is mediated by the gluon, which as discussed above also carries
274 the strong color charge. There is the fundamental three-point interaction, where a
275 quark radiates a gluon. Additionally, there are the three-point and four-point gluon-
276 only interactions.

277 2.3 Deficiencies of the Standard Model

278 At this point, it is quite easy to simply rest on our laurels. This relatively simple
279 theory is capable of explaining a very wide range of phenomena, which ultimately
280 break down only to combinations of nine diagrams shown in Fig.2.3. Unfortunately,
281 there are some unexplained problems with the Standard Model. We cannot go
282 through all of the potential issues in this thesis, but we will motivate the primary
283 issues which naturally lead one to *supersymmetry*, as we will see in Ch.3.

The Standard Model has many free parameters; see Table 2.1 In general, we prefer models with less free parameters. A great example of this fact, and the primary experimental evidence for EWSB, is the relationship between the couplings of the weak force and the masses of the gauge bosons of the weak force :

$$\rho \equiv \frac{m_W^2}{m_Z^2 \cos^2 \theta_W} \stackrel{?}{=} 1 \quad (2.16)$$

284 where ? indicates that this is a testable prediction of the Standard Model (in
285 particular, that the gauge bosons gain mass through EWSB). This relationship has
286 been measured within experimental and theoretical predictions. We would like to
287 produce additional such relationships, which would exist if the Standard Model is a
288 low-energy approximation of some other theory.

289 An additional issue is the lack of *gauge coupling unification*. The couplings of
290 any quantum field theory “run” as a function of the distance scales (or inversely,

Table 2.1: Parameters of the Standard Model. For values dependent on the renormalization scheme, we use a combination of the on-shell normalization scheme [59–62] and modified minimal subtraction scheme with $m_{\bar{MS}}$ as indicated in the table[63]

m_e	Electron mass	511 keV
m_μ	Muon mass	105.7 MeV
m_τ	Tau mass	1.78 GeV
m_u	Up quark mass	1.9 MeV ($m_{\bar{MS}} = 2\text{GeV}$)
m_d	Down quark mass	4.4 MeV ($m_{\bar{MS}} = 2\text{GeV}$)
m_s	Strange quark mass	87 MeV ($m_{\bar{MS}} = 2\text{GeV}$)
m_c	Charm quark mass	1.32 GeV ($m_{\bar{MS}} = m_c$)
m_b	Bottom quark mass	4.24 GeV ($m_{\bar{MS}} = m_b$)
m_t	Top quark mass	172.7 GeV (on-shell renormalization)
θ_{12} CKM	12-mixing angle	13.1°
θ_{23} CKM	23-mixing angle	2.4°
θ_{13} CKM	13-mixing angle	0.2°
δ CKM	CP-violating Phase	0.995
g'	U(1) gauge coupling	0.357 ($m_{\bar{MS}} = m_Z$)
g	SU(2) gauge coupling	0.652 ($m_{\bar{MS}} = m_Z$)
g_s	SU(3) gauge coupling	1.221 ($m_{\bar{MS}} = m_Z$)
θ_{QCD}	QCD vacuum angle	~0
VEV	Higgs vacuum expectation value	246 GeV
m_H	Higgs mass	125 GeV

291 energy scales) of the theory. The idea is closely related to the unification of the
 292 electromagnetic and weak forces at the so-called *electroweak scale* of $O(100 \text{ GeV})$.

293 One would hope this behavior was repeated between the electroweak forces and the
 294 strong force at some suitable energy scale. The Standard Model does automatically
 295 not exhibit this behavior, as we can see in Fig.2.4.

The most significant problem with the Standard Model is the *hierarchy problem*. In its most straightforward incarnation, the Higgs scalar field is subject to quantum corrections through loop diagrams, as shown in Fig.2.5. For demonstration, we use the contributions from the top quark, since the top quark has the largest Higgs Yukawa coupling due to its large mass. In general, we should expect these corrections to quadratically depend on the scale of the ultraviolet physics, Λ . Briefly assume there is no new physics before the Planck scale of gravity, $\Lambda_{\text{Planck}} = 10^{19} \text{ GeV}$. In this

Figure 2.4: The running of Standard Model gauge couplings. The Standard Model couplings do not unify at high energies, which indicates it cannot completely describe nature through the Planck scale.

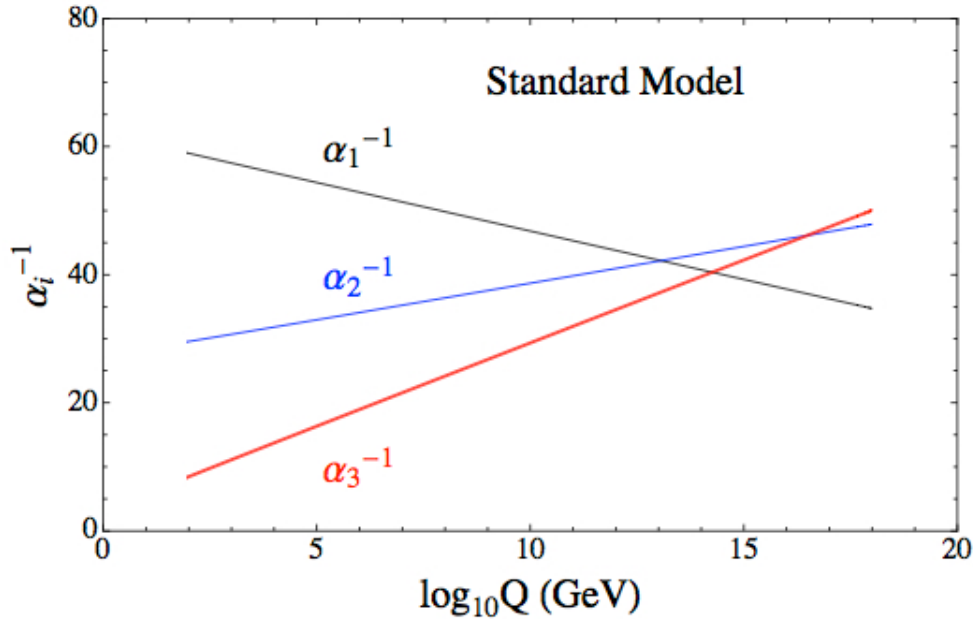
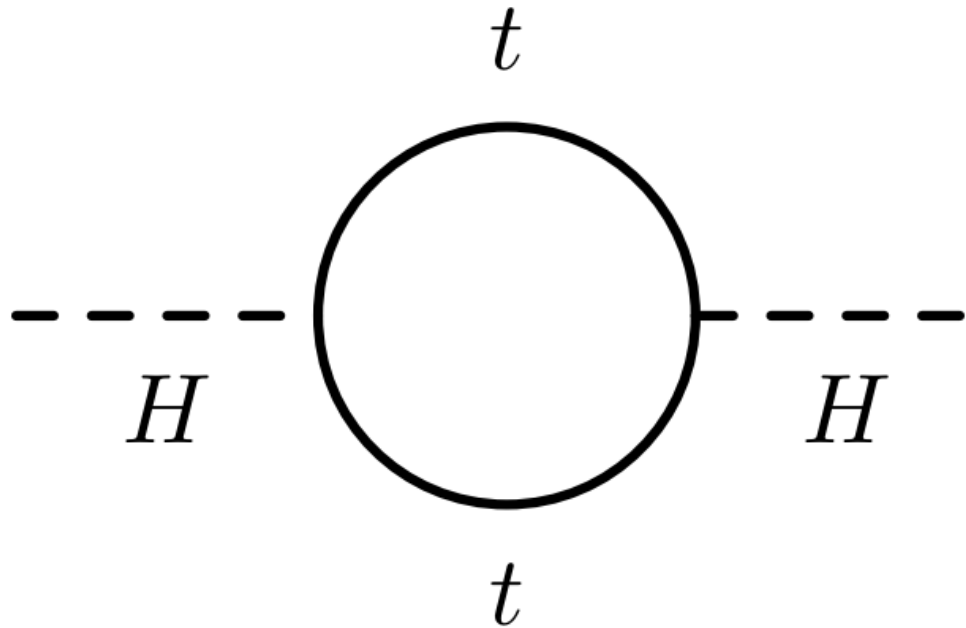


Figure 2.5: The dominant quantum loop correction to the Higgs mass in the Standard Model.



case, we expect the corrections to the Higgs mass like

$$\delta m_H^2 \approx \left(\frac{m_t}{8\pi^2 \langle \phi \rangle_{VEV}} \right)^2 \Lambda_{Planck}^2. \quad (2.17)$$

296 To achieve the miraculous cancellation required to get the observed Higgs mass of
297 125 GeV, one needs to then set the bare Higgs mass m_0 , our input to the Standard
298 Model Lagrangian, itself to a *precise* value $\sim 10^{19}$ GeV. This extraordinary level of
299 parameter finetuning is quite undesirable, and within the framework of the Standard
300 Model, there is little that can be done to alleviate this issue.

301 An additional concern, of a different nature, is the lack of a *dark matter* candidate
302 in the Standard Model. Dark matter was discovered by observing galactic rotation
303 curves, which showed that much of the matter that interacted gravitationally was
304 invisible to our (electromagnetic) telescopes [16–22]. The postulation of the existence
305 of dark matter, which interacts at least through gravity, allows one to understand
306 these galactic rotation curves. Unfortunately, no particle in the Standard Model could
307 possibly be the dark matter particle. The only candidate truly worth another look is
308 the neutrino, but it has been shown that the neutrino content of the universe is simply
309 too small to explain the galactic rotation curves [22, 64]. The experimental evidence
310 from the galactic rotations curves thus show there *must* be additional physics beyond
311 the Standard Model, which is yet to be understood.

312 In the next chapter, we will see how these problems can be alleviated by the theory
313 of supersymmetry.

Figure 2.6: Particles of the Standard Model

mass → $\approx 2.3 \text{ MeV}/c^2$	charge → $2/3$	spin → $1/2$	mass → $\approx 1.275 \text{ GeV}/c^2$	charge → $2/3$	spin → $1/2$	mass → $\approx 173.07 \text{ GeV}/c^2$	charge → $2/3$	spin → $1/2$	mass → 0	charge → 0	spin → 1	mass → $\approx 126 \text{ GeV}/c^2$	charge → 0	spin → 0
u	c	t	g	H										
up	charm	top	gluon	Higgs boson										
d	s	b	γ											
down	strange	bottom	photon											
e	μ	τ	Z											
electron	muon	tau	Z boson											
ν_e	ν_μ	ν_τ	W											
electron neutrino	muon neutrino	tau neutrino	W boson											

Supersymmetry

316 This chapter will introduce supersymmetry (SUSY) [15, 23–35]. We will begin by
 317 introducing the concept of a *superspace*, and discuss some general ingredients of
 318 supersymmetric theories. This will include a discussion of how the problems with the
 319 Standard Model described in Ch.2 are naturally fixed by these theories.

320 The next step is to discuss the particle content of the *Minimally Supersymmetric*
 321 *Standard Model* (MSSM). As its name implies, this theory contains the minimal
 322 additional particle content to make Standard Model supersymmetric. We then discuss
 323 the important phenomenological consequences of this theory, especially as it would
 324 be observed in experiments at the LHC.

325 **3.1 Supersymmetric theories : from space to
 326 superspace**

327 **Coleman-Mandula “no-go” theorem**

328 We begin the theoretical motivation for supersymmetry by citing the “no-go” theorem
 329 of Coleman and Mandula [65]. This theorem forbids *spin-charge unification*; it
 330 states that all quantum field theories which contain nontrivial interactions must be
 331 a direct product of the Poincaré group of Lorentz symmetries, the internal product
 332 from of gauge symmetries, and the discrete symmetries of parity, charge conjugation,
 333 and time reversal. The assumptions which go into building the Coleman-Mandula

theorem are quite restrictive, but there is one unique way out, which has become known as *supersymmetry* [26, 66]. In particular, we must introduce a *spinorial* group generator Q . Alternatively, and equivalently, this can be viewed as the addition of anti-commuting coordinates; space plus these new anti-commuting coordinates is then called *superspace* [67]. We will not investiage this view in detail, but it is also a quite intuitive and beautiful way to construct supersymmetry[15].

340 Supersymmetry transformations

A *supersymmetric* transformation Q transforms a bosonic state into a fermionic state, and vice versa :

$$Q |\text{Fermion}\rangle = |\text{Boson}\rangle \quad (3.1)$$

$$Q |\text{Boson}\rangle = |\text{Fermion}\rangle \quad (3.2)$$

To ensure this relation holds, Q must be an anticommuting spinor. Additionally, since spinors are inherently complex, Q^\dagger must also be a generator of the supersymmetry transformation. Since Q and Q^\dagger are spinor objects (with $s = 1/2$), we can see that supersymmetry must be a spacetime symmetry. The Haag-Lopuszanski-Sohnius extension [66] of the Coleman-Mandula theorem [65] is quite restrictive about the forms of such a symmetry. Here, we simply write the (anti-) commutation relations [15] :

$$Q_\alpha, Q_{\dot{\alpha}}^\dagger = -2\sigma_{\alpha\dot{\alpha}\mu} P_\mu \quad (3.3)$$

$$Q_\alpha, Q_{\dot{\beta}} = Q_{\dot{\alpha}}^\dagger, Q_{\dot{\beta}}^\dagger = 0 \quad (3.4)$$

$$[P^\mu, Q_\alpha] = [P^\mu, Q_{\dot{\alpha}}^\dagger] = 0 \quad (3.5)$$

343 **Supermultiplets**

344 In a supersymmetric theory, we organize single-particle states into irreducible
345 representations of the supersymmetric algebra which are known as *supermultiplets*.
346 Each supermultiplet contains a fermion state $|F\rangle$ and a boson state $|B\rangle$; these two
347 states are the known as *superpartners*. These are related by some combination of
348 Q and Q^\dagger , up to a spacetime transformation. Q and Q^\dagger commute with the mass-
349 squared operator $-P^2$ and the operators corresponding to the gauge transformations
350 [15]; in particular, the gauge interactions of the Standard Model. In an unbroken
351 supersymmetric theory, this means the states $|F\rangle$ and $|B\rangle$ have exactly the same mass,
352 electromagnetic charge, electroweak isospin, and color charges. One can also prove
353 [15] that each supermultiplet contains the exact same number of bosonic (n_B) and
354 fermion (n_F) degrees of freedom. We now explore the possible types of supermultiples
355 one can find in a renormalizable supersymmetric theory.

356 Since each supermultiplet must contain a fermion state, the simplest type of
357 supermultiplet contains a single Weyl fermion state ($n_F = 2$) which is paired with
358 $n_B = 2$ scalar bosonic degrees of freedom. This is most conveniently constructed as
359 single complex scalar field. We call this construction a *scalar supermultiplet* or *chiral*
360 *supermultiplet*. The second name is indicative; only chiral supermultiplets can contain
361 fermions whose right-handed and left-handed components transform differently under
362 the gauge interactions (as of course happens in the Standard Model).

363 The second type of supermultiplet we construct is known as a *gauge* supermul-
364 tiplet. We take a spin-1 gauge boson (which must be massless due to the gauge
365 symmetry, so $n_B = 2$) and pair this with a single massless Weyl spinor¹. The gauge
366 bosons transform as the adjoint representation of the their respective gauge groups;
367 their fermionic partners, which are known as gauginos, must also. In particular,
368 the left-handed and right-handed components of the gaugino fermions have the same

¹Choosing an $s = 3/2$ massless fermion leads to nonrenormalizable interactions.

369 gauge transformation properties.

370 Excluding gravity, this is the entire list of supermultiplets which can participate
371 in renormalizable interactions in what is known as $N = 1$ supersymmetry. This
372 means there is only one copy of the supersymmetry generators Q and Q^\dagger . This is
373 essentially the only “easy” phenomenological choice, since it is the only choice in four
374 dimensions which allows for the chiral fermions and parity violations built into the
375 Standard Model, and we will not look further into $N > 1$ supersymmetry in this thesis.

376 The primary goal, after understanding the possible structures of the multiplets
377 above, is to fit the Standard Model particles into a multiplet, and therefore make
378 predictions about their supersymmetric partners. We explore this in the next section.

379 **3.2 Minimally Supersymmetric Standard Model**

380 To construct what is known as the MSSM [[susyPrimer](#) , 68–71], we need a few
381 ingredients and assumptions. First, we match the Standard Model particles with
382 their corresponding superpartners of the MSSM. We will also introduce the naming
383 of the superpartners (also known as *sparticles*). We discuss a very common additional
384 restraint imposed on the MSSM, known as R –parity. We also discuss the concept of
385 soft supersymmetry breaking and how it manifests itself in the MSSM.

386 **Chiral supermultiplets**

387 The first thing we deduce is directly from Sec.?? . The bosonic superpartners
388 associated to the quarks and leptons *must* be spin 0, since the quarks and leptons must
389 be arranged in a chiral supermultiplet. This is essentially the note above, since the
390 chiral supermultiplet is the only one which can distinguish between the left-handed
391 and right-handed components of the Standard Model particles. The superpartners of
392 the quarks and leptons are known as *squarks* and *sleptons*, or *sfermions* in aggregate.

393 (for ‘‘scalar quarks’’, ‘‘scalar leptons’’, and ‘‘scalar fermion’’²). The ‘‘s-’’ prefix
 394 can also be added to the individual quarks i.e. *selectron*, *sneutrino*, and *stop*. The
 395 notation is to add a \sim over the corresponding Standard Model particle i.e. \tilde{e} , the
 396 selectron is the superpartner of the electron. The two-component Weyl spinors of the
 397 Standard Model must each have their own (complex scalar) partner i.e. e_L, e_R have
 398 two distinct partners : \tilde{e}_L, \tilde{e}_R . As noted above, the gauge interactions of any of the
 399 sfermions are identical to those of their Standard Model partners.

Due to the scalar nature of the Higgs, it must obviously lie in a chiral supermultiplet. To avoid gauge anomalies and ensure the correct Yukawa couplings to the quarks and leptons[15], we must add additional Higgs bosons to any supersymmetric theory. In the MSSM, we have two chiral supermultiplets. The SM (SUSY) parts of the multiplets are denoted $H_u(\tilde{H}_u)$ and $H_d(\tilde{H}_d)$. Writing out H_u and H_d explicitly:

$$H_u = \begin{pmatrix} H_u^+ \\ H_u^0 \end{pmatrix} \quad (3.6)$$

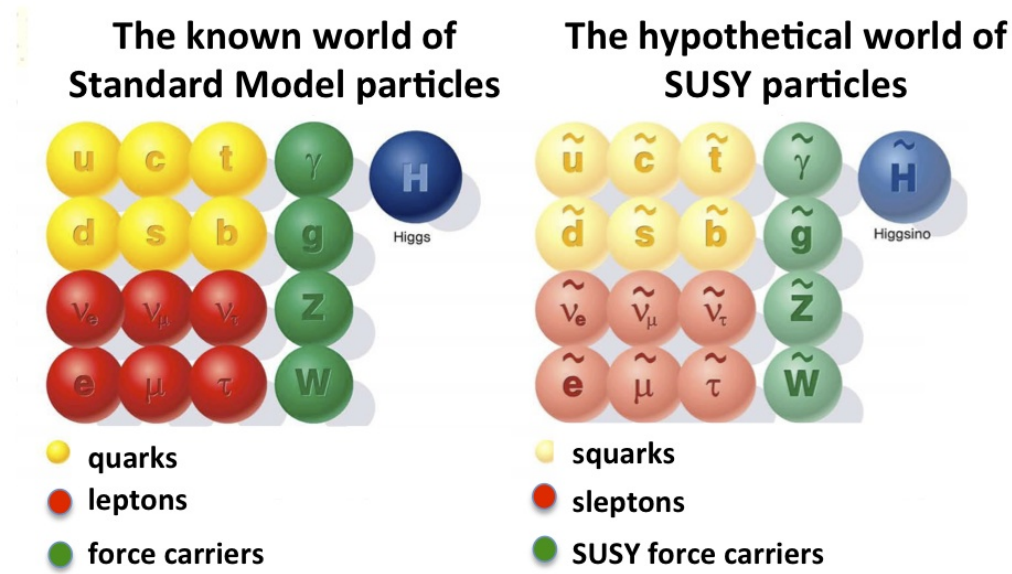
$$H_d = \begin{pmatrix} H_d^0 \\ H_d^- \end{pmatrix} \quad (3.7)$$

(3.8)

400 we see that H_u looks very similar to the SM Higgs with $Y = 1$, and H_d is symmetric
 401 to this with $+ \rightarrow -$, with $Y = -1$. The SM Higgs boson, h_0 , is a linear superposition
 402 of the neutral components of these two doublets. The SUSY parts of the Higgs
 403 multiplets, \tilde{H}_u and \tilde{H}_d , are each left-handed Weyl spinors. For generic spin-1/2
 404 sparticles, we add the ‘‘-ino’’ suffix. We then call the partners of the two Higgs
 405 collectively the *Higgsinos*.

²The last one should probably have bigger scare quotes.

Figure 3.1: Particles of the MSSM



406 Gauge supermultiplets

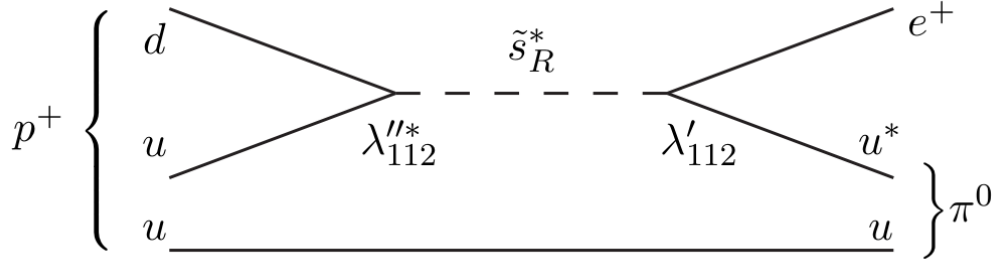
407 The superpartners of the gauge bosons must all be in gauge supermultiplets since
 408 they contain a spin-1 particle. Collectively, we refer to the superpartners of the
 409 gauge bosons as the gauginos.

410 The first gauge supermultiplet contains the gluon, and its superpartner, which is
 411 known as the *gluino*, denoted \tilde{g} . The gluon is of course the SM mediator of $SU(3)_C$;
 412 the gluino is also a colored particle, subject to $SU(3)_C$. From the SM before EWSB,
 413 we have the four gauge bosons of the electroweak symmetry group $SU(2)_L \otimes U(1)_Y$:
 414 $W^{1,2,3}$ and B^0 . The superpartners of these particles are thus the *winos* $W^{\tilde{1},\tilde{2},\tilde{3}}$ and
 415 *bino* \tilde{B}^0 , where each is placed in another gauge supermultiplet with its corresponding
 416 SM particle. After EWSB, without breaking supersymmetry, we would also have the
 417 zino \tilde{Z}^0 and photino $\tilde{\gamma}$.

418 The entire particle content of the MSSM can be seen in Fig.3.1.

419 At this point, it's important to take a step back. Where are these particles?
 420 As stated above, supersymmetric theories require that the masses and all quantum

Figure 3.2: This Feynmann diagram shows how proton decay is induced in the MSSM, if one does not impose R -parity.



421 numbers of the SM particle and its corresponding sparticle are the same. Of course,
 422 we have not observed a selectron, squark, or wino. The answer, as it often is, is that
 423 supersymmetry is *broken* by the vacuum state of nature [15].

424 **R -parity**

This section is a quick aside to the general story. R – parity refers to an additional discrete symmetry which is often imposed on supersymmetric models. For a given particle state, we define

$$R = (-1)^{3(B-L)+2s} \quad (3.9)$$

425 where B, L is the baryon (lepton) number and s is the spin. The imposition of
 426 this symmetry forbids certain terms from the MSSM Lagrangian that would violate
 427 baryon and/or lepton number. This is required in order to prevent proton decay, as
 428 shown in Fig.3.2³. .

429 In supersymmetric models, this is a \mathbb{Z}_2 symmetry, where SM particles have $R = 1$
 430 and sparticles have $R = -1$. We will take R – parity as part of the definition of
 431 the MSSM. We will discuss later the *drastic* consequences of this symmetry on SUSY
 432 phenomenology

³Proton decay can actually be prevented by allowing only one of the four potential R-parity violating terms to survive.

433 **Soft supersymmetry breaking**

The fundamental idea of *soft* supersymmetry breaking[15, 34, 35, 72, 73] is that we would like to break supersymmetry without reintroducing the quadratic divergences we discussed at the end of Chapter 2. We write the Lagrangian in a form :

$$\mathcal{L}_{\text{MSSM}} = \mathcal{L}_{\text{SUSY}} + \mathcal{L}_{\text{soft}} \quad (3.10)$$

434 In this sense, the symmetry breaking is “soft”, since we have separated out the
 435 completely symmetric terms from those soft terms which will not allow the quadratic
 436 divergences to the Higgs mass.

437 The explicitly allowed terms in the soft-breaking Lagrangian are [35].

- 438 • Mass terms for the scalar components of the chiral supermultipletss
 439 • Mass terms for the Weyl spinor components of the gauge supermultipletss
 440 • Trilinear couplings of scalar components of chiral supermultiplets

In particular, using the field content described above for the MSSM, the softly-broken portion of the MSSM Lagrangian can be written

$$\mathcal{L}_{\text{soft}} = -\frac{1}{2} \left(M_3 \tilde{g} \tilde{g} + M_2 \tilde{W} \tilde{W} + M_1 \tilde{B} \tilde{B} + c.c. \right) \quad (3.11)$$

$$- \left(\tilde{u} a_u \tilde{Q} H_u - \tilde{d} a_d \tilde{Q} H_d - \tilde{e} a_e \tilde{L} H_d + c.c. \right) \quad (3.12)$$

$$- \tilde{Q}^\dagger m_Q^2 \tilde{Q} - \tilde{L}^\dagger m_L^2 \tilde{L} - \tilde{u} m_u^2 \tilde{u}^\dagger - \tilde{d} m_d^2 \tilde{d}^\dagger - \tilde{e} m_e^2 \tilde{e}^\dagger \quad (3.13)$$

$$- m_{H_u}^2 H_u^* H_u - m_{H_d}^2 H_d^* H_d - (b H_u H_d + cc). \quad (3.14)$$

441 where we have introduced the following notations :

442 1. M_3, M_2, M_1 are the gluino, wino, and bino masses.

443 2. a_u, a_d, a_e are complex 3×3 matrices in family space.

444 3. $m_Q^2, m_u^2, m_d^2, m_L^2, m_e^2$ are hermitian 3×3 matrices in family space.

445 4. $m_{H_u}^2, m_{H_d}^2, b$ are the SUSY-breaking contributions to the Higgs potential.

446 We have written matrix terms without any sort of additional notational decoration
 447 to indicate their matrix nature, and we now show why. The first term 1 are
 448 straightforward; these are just the straightforward mass terms for these fields. There
 449 are strong constraints on the off-diagonal terms for the matrices of 2 [74, 75]; for
 450 simplicity, we will assume that each $a_i, i = u, d, e$ is proportional to the Yukawa
 451 coupling matrix : $a_i = A_{i0}y_i$. The matrices in ?? can be similarly constrained by
 452 experiments [68, 75–82] Finally, we assume that the elements 4 contributing to the
 453 Higgs potential as well as all of the 1 terms must be real, which limits the possible
 454 CP-violating interactions to those of the Standard Model. We thus only consider
 455 flavor-blind, CP-conserving interactions within the MSSM.

The important mixing for mass and gauge interaction eigenstates in the MSSM occurs within electroweak sector, in a process akin to EWSB in the Standard Model. The neutral portions of the Higgsinos doublets and the neutral gauginos ($\tilde{H}_u^0, \tilde{H}_d^0, \tilde{B}^0, \tilde{W}^0$) of the gauge interaction basis mix to form what are known as the *neutralinos* of mass basis :

$$M_{\tilde{\chi}} = \begin{pmatrix} M_1 & 0 & -c_\beta s_W m_Z & s_\beta s_W m_Z \\ 0 & M_2 & c_\beta c_W m_Z & -s_\beta c_W m_Z \\ -c_\beta s_W m_Z & c_\beta c_W m_Z & 0 & -\mu \\ s_\beta s_W m_Z & -s_\beta c_W m_Z & -\mu & 0 \end{pmatrix} \quad (3.15)$$

456 where $s(c)$ are the sine and cosine of angles related to EWSB, which introduced
 457 masses to the gauginos and higgsinos. Diagonalization of this matrix gives the four
 458 neutralino mass states, listed without loss of generality in order of increasing mass :
 459 $\tilde{\chi}_{1,2,3,4}^0$.

460 The neutralinos, especially the lightest neutralino $\tilde{\chi}_1^0$, are important ingredients
 461 in SUSY phenomenology.

462 The same process can be done for the electrically charged gauginos with
463 the charged portions of the Higgsino doublets along with the charged winos
464 $(\tilde{H}_u^+, \tilde{H}_d^+, \tilde{W}^+, \tilde{W}^-)$. This leads to the *charginos*, again in order of increasing mass
465 : $\tilde{\chi}_{1,2}^\pm$.

466

3.3 Phenomenology

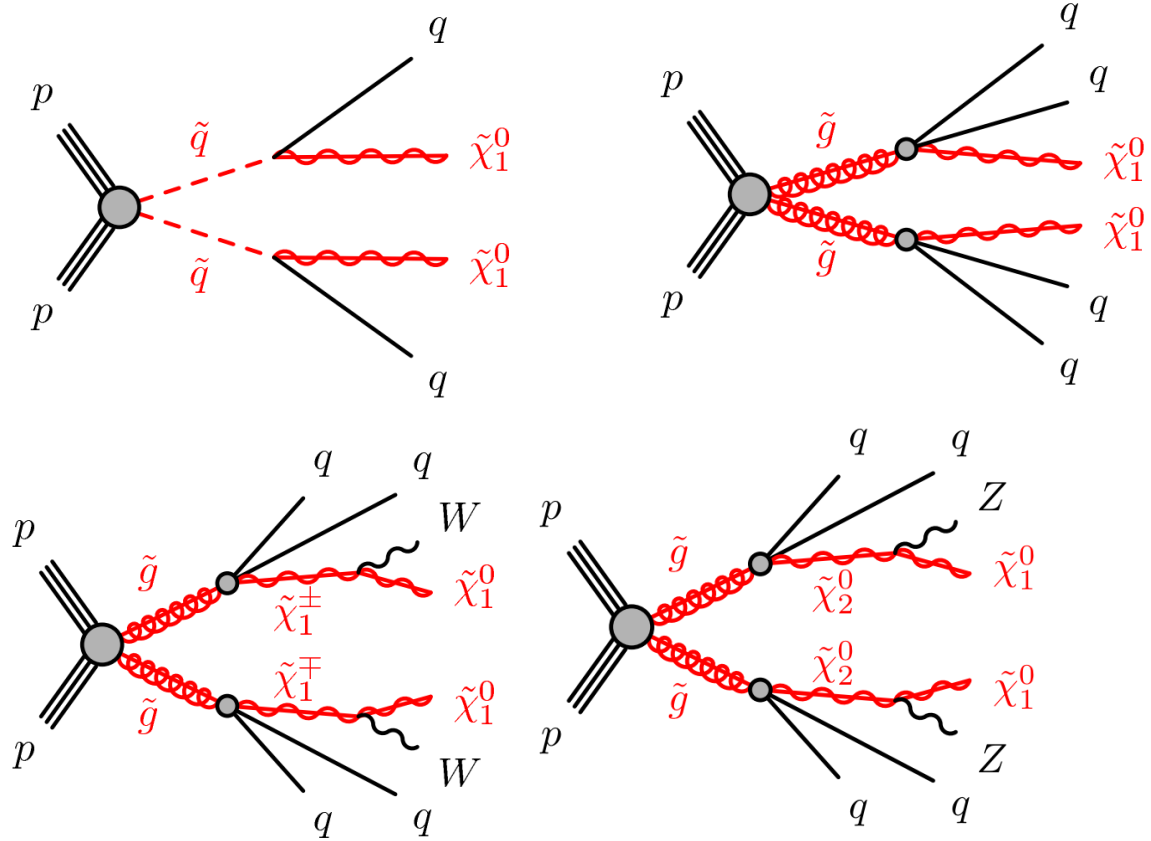
467 We are finally at the point where we can discuss the phenomenology of the MSSM,
468 in particular as it manifests itself at the energy scales of the LHC.

469 As noted above in Sec.3.2, the assumption of *R*–parity has important conse-
470 quences for MSSM phenomenology. The SM particles have $R = 1$, while the sparticles
471 all have $R = -1$. Simply, this is the “charge” of supersymmetry. Since the particles of
472 LHC collisions (pp) have total incoming $R = 1$, we must expect that all sparticles will
473 be produced in *pairs*. An additional consequence of this symmetry is the fact that the
474 lightest supersymmetric particle (LSP) is *stable*. Off each branch of the Feynmann
475 diagram shown in Fig., we have $R = -1$, and this can only decay to another sparticle
476 and a SM particle. Once we reach the lightest sparticle in the decay, it is absolutely
477 stable. This leads to the common signature E_T^{miss} for a generic SUSY signal.

478 For this thesis, we will be presenting an inclusive search for squarks and gluinos
479 with zero leptons in the final state. This is a very interesting decay channel⁴, due
480 to the high cross-sections of $\tilde{g}\tilde{g}$ and $\tilde{q}\tilde{q}$ decays, as can be seen in Fig.?? [83]. This
481 is a direct consequence of the fact that these are the colored particles of the MSSM.
482 Since the sparticles interact with the gauge groups of the SM in the same way as their
483 SM partners, the colored sparticles, the squarks and gluinos, are produced and decay
484 as governed by the color group $SU(3)_C$ with the strong coupling g_S . The digluino
485 production is particularly copious, due to color factor corresponding to the color octet

⁴Prior to Run1, probably the most *most* interesting SUSY decay channel.

Figure 3.3: SUSY signals considered in this thesis



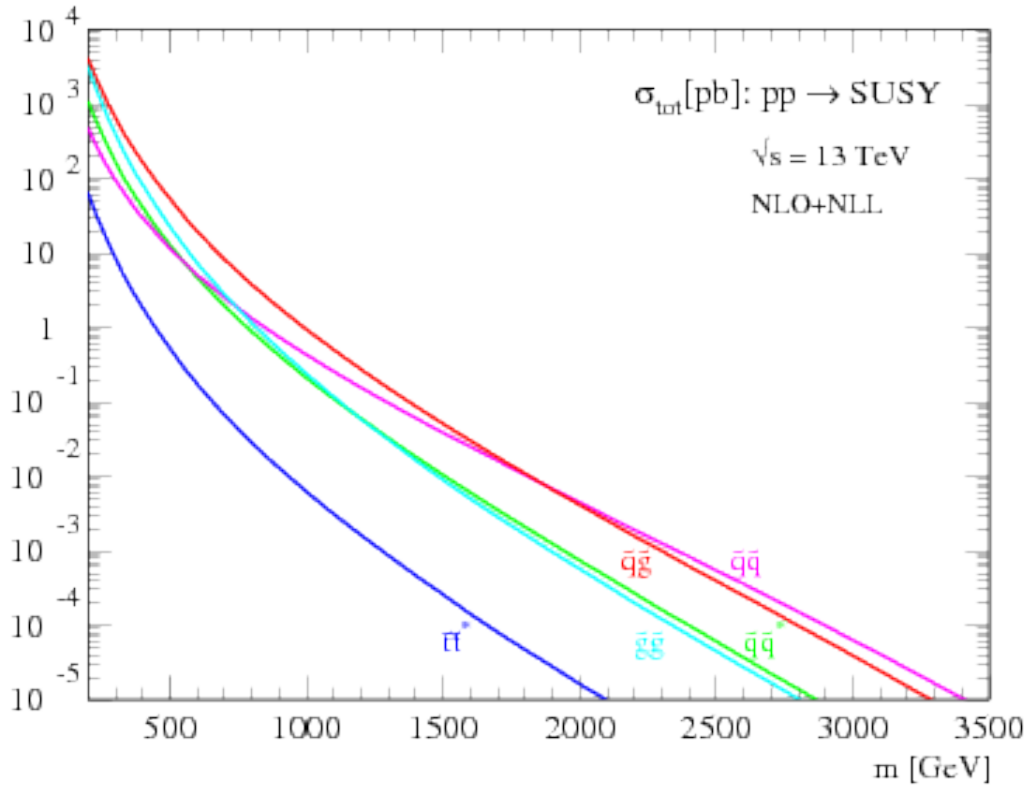
486 of $SU(3)C$.

487 In the case of disquark production, the most common decay mode of the squark in
 488 the MSSM is a decay directly to the LSP plus a single SM quark [15]. This means the
 489 basic search strategy of disquark production is two jets from the final state quarks,
 490 plus missing transverse energy for the LSPs. There are also cascade decays, the most
 491 common of which, and the only one considered in this thesis, is $\tilde{q} \rightarrow q\chi_1^\pm \rightarrow qW^\pm\chi_1^0$.

492 For digluino production, the most common decay is $\tilde{g} \rightarrow g\tilde{q}$, due to the large
 493 g_S coupling. The squark then decays as listed above. In this case, we generically
 494 search for four jets and missing transverse energy from the LSPs. We can also have
 495 the squark decay in association with a W^\pm or Z^0 ; in this thesis, we are interested in
 496 those cases where this vector boson goes hadronically.

497 In the context of experimental searches for SUSY, we often consider *simplified*

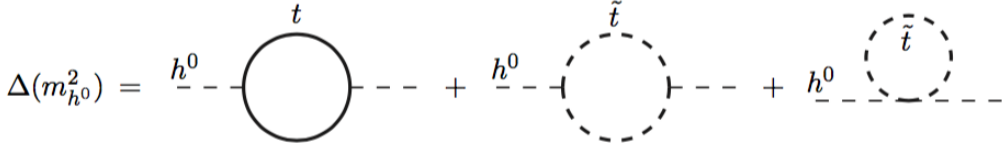
Figure 3.4: SUSY production cross-sections as a function of sparticle mass at $\sqrt{s} = 13$ TeV.



498 *models*. These models make certain assumptions which allow easy comparisons of
 499 results by theorists and rival experimentalists. In the context of this thesis, the
 500 simplified models will make assumptions about the branching ratios described in the
 501 preceding paragraphs. In particular, we will often choose a model where the decay of
 502 interest occurs with 100% branching ratio. This is entirely for ease of interpretation
 503 by other physicists⁵, but it is important to recognize that these are more a useful
 504 comparison tool, especially with limits, than a strict statement about the potential
 505 masses of sought-after beyond the Standard Model particle.

⁵In the author's opinion, this often leads to more confusion than comprehension. We will revisit the shortcomings of simplified models in the Conclusion to this thesis.

Figure 3.5: Loop diagrams correct the Higgs mass in the MSSM



506 3.4 How SUSY solves the problems with the SM

507 We now return to the issues with the Standard Model as described in Ch.2 to see
508 how these issues are solved by supersymmetry.

509 Quadratic divergences to the Higgs mass

The quadratic divergences induced by the loop corrections to the Higgs mass, for example from the top Yukawa coupling, goes as

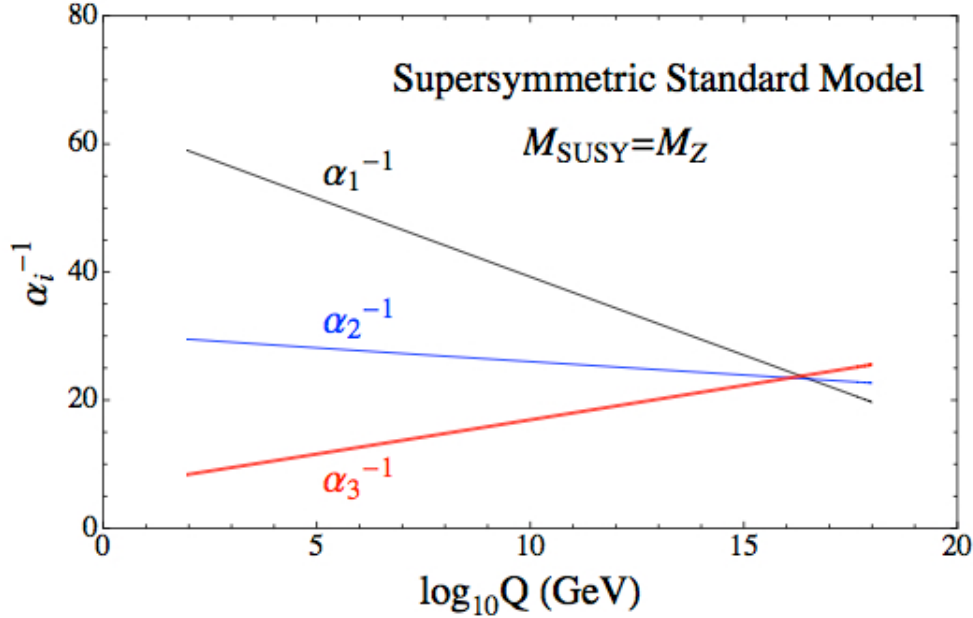
$$\delta m_H^2 \approx \left(\frac{m_t}{8\pi^2 \langle \phi \rangle_{VEV}} \right)^2 \Lambda_{Planck}^2. \quad (3.16)$$

510 The miraculous thing about SUSY is each of these terms *automatically* comes
511 with a term which exactly cancels this contribution[15]. The fermions and bosons
512 have opposite signs in this loop diagram to all orders in perturbation theory, which
513 completely solves the hierarchy problem. This is the most well-motivated reason for
514 supersymmetry.

515 Gauge coupling unification

516 An additional motivation for supersymmetry is seen by the gauge coupling unification
517 high scales. In the Standard Model, as we saw the gauge couplings fail to unify at
518 high energies. In the MSSM and many other forms of supersymmetry, the gauge
519 couplings unify at high energy, as can be seen in Fig.???. This provides additional
520 aesthetic motivation for supersymmetric theories.

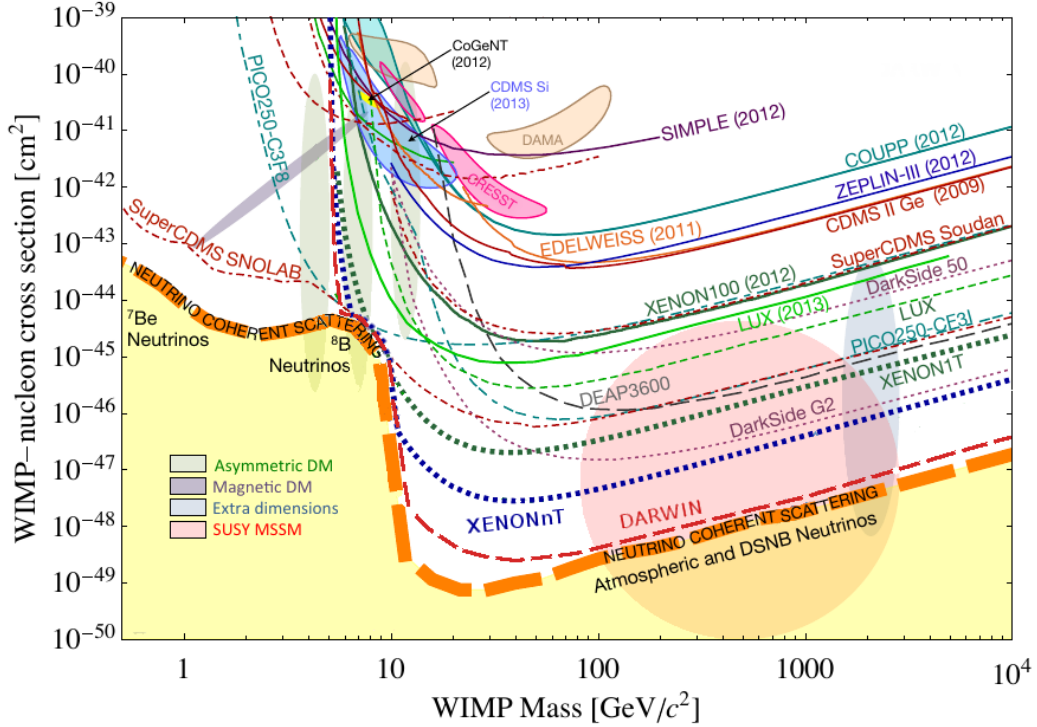
Figure 3.6: The running of Standard Model gauge couplings; compare to Fig.2.4. The MSSM gauge couplings nearly intersect at high energies.



521 Dark matter

522 As we discussed previously, the lack of any dark matter candidate in the Standard
 523 Model naturally leads to beyond the Standard Model theories. In the Standard Model,
 524 there is a natural dark matter candidate in the lightest supersymmetric particle[15]
 525 The LSP would in dark matter experiments be called a *weakly-interacting massive*
 526 *particle* (WIMP), which is a type of cold dark matter [22, 84]. These WIMPS would
 527 only interact through the weak force and gravity, which is exactly as a model like the
 528 MSSM predicts for the neutralino. In Fig.3.7, we can see the current WIMP exclusions
 529 for a given mass. The range of allowed masses which have not been excluded for LSPs
 530 and WIMPs have significant overlap. This provides additional motivation outside of
 531 the context of theoretical details.

Figure 3.7: WIMP exclusions from direct dark matter detection experiments.



532 3.5 Conclusions

533 Supersymmetry is the most well-motivated theory for physics beyond the Standard
 534 Model. It provides a solution to the hierarchy problem, leads to gauge coupling
 535 unification, and provides a dark matter candidate consistent with galactic rotation
 536 curves. As noted in this chapter, due to the LSPs in the final state, most SUSY
 537 searches require a significant amount of missing transverse energy in combination
 538 with jets of high transverse momentum. However, there is some opportunity to do
 539 better than this, especially in final states where one has two weakly-interacting LSPs
 540 on opposite sides of some potentially complicated decay tree. We will see how this is
 541 done in Ch.??.

The Large Hadron Collider

544 The Large Hadron Collider (LHC) produces high-energy protons which are collided
 545 at the center of multiple large experiments at CERN on the outskirts of Geneva,
 546 Switzerland [85]. The LHC produces the highest energy collisions in the world,
 547 with design center-of-mass energy of $\sqrt{s} = 14$ TeV, which allows the experiments
 548 to investigate physics far beyond the reach of previous colliders. This chapter will
 549 summarize the basics of accelerator physics, especially with regards to discovering
 550 physics beyond the Standard Model. We will describe the CERN accelerator complex
 551 and the LHC.

552 **4.1 Basics of Accelerator Physics**

553 This section follows closely the presentation of [86].

Simple particle accelerators simply rely on the acceleration of charged particles in a static electric field. Given a field of strength E , charge q , and mass m , this is simply

$$a = \frac{qE}{m}. \quad (4.1)$$

554 For a given particle with a given mass and charge, this is limited by the static electric
 555 field which can be produced, which in turn is limited by electrical breakdown at high
 556 voltages.

557 There are two complementary solutions to this issue. First, we use the *radio*
 558 *frequency acceleration* technique. We call the devices used for this *RF cavities*. The

559 cavities produce a time-varied electric field, which oscillate such that the charged
 560 particles passing through it are accelerated towards the design energy of the RF
 561 cavity. This oscillation also induces the particles into *bunches*, since particles which
 562 are slightly off in energy from that induced by the RF cavity are accelerated towards
 563 the design energy.

Second, one bends the particles in a magnetic field, which allows them to pass through the same RF cavity over and over. This second process is often limited by *synchrotron radiation*, which describes the radiation produced when a charged particle is accelerated. The power radiated is

$$P \sim \frac{1}{r^2} \left(E/m \right)^4 \quad (4.2)$$

564 where r is the radius of curvature and E, m is the energy (mass) of the charged
 565 particle. Given an energy which can be produced by a given set of RF cavities (which
 566 is *not* limited by the mass of the particle), one then has two options to increase the
 567 actual collision energy : increase the radius of curvature or use a heavier particle.
 568 Practically speaking, the easiest options for particles in a collider are protons and
 569 electrons, since they are (obviously) copious in nature and do not decay¹. Given the
 570 dependence on mass, we can see why protons are used to reach the highest energies.
 571 The tradeoff for this is that protons are not point particles, and we thus we don't
 572 know the exact incoming four-vectors of the protons, as discussed in Ch.2.

The particle *beam* refers to the bunches all together An important property of a beam of a particular energy E , moving in uniform magnetic field B , containing particles of momentum p is the *beam rigidity* :

$$R \equiv rB = p/c. \quad (4.3)$$

573 The linear relation between r and p , or alternatively B and p have important
 574 consequences for LHC physics. For hadron colliders, this is the limiting factor on

¹Muon colliders are a really cool option at high energies, since the relativistic γ factor gives them a relatively long lifetime in the lab frame.

575 going to higher energy scales; one needs a proportionally larger magnetic field to
576 keep the beam accelerating in a circle.

577 Besides the rigidity of the beam, the most important quantities to characterize
578 a beam are known as the (normalized) *emittance* ϵ_N and the *betatron function* β .
579 These quantities determine the transverse size σ of a relativistic beam $v \gtrsim c$ beam :
580 $\sigma^2 = \beta^* \epsilon_N / \gamma_{\text{rel}}$, where β^* is the value of the betatron function at the collision point
581 and γ_{rel} is the Lorentz factor.

These quantities determine the *instantaneous luminosity* L of a collider, which combined with the cross-section σ of a particular physics process, give the rate of this physics process :

$$R = L\sigma. \quad (4.4)$$

The instantaneous luminosity L is given by :

$$L = \frac{f_{\text{rev}} N_b^2 F}{4\pi\sigma^2} = \frac{f_{\text{rev}} n N_b^2 \gamma_{\text{rel}} F}{4\pi\beta^* \epsilon_N}. \quad (4.5)$$

582 Here we have introduced the frequency of revolutions f_{rev} , the number of bunches n ,
583 the number of protons per bunch N_b^2 , and a geometric factor F related to the crossing
584 angle of the beams.

The *integrated luminosity* $\int L$ gives the total number of a particular physics process P , with cross-section σ_P .

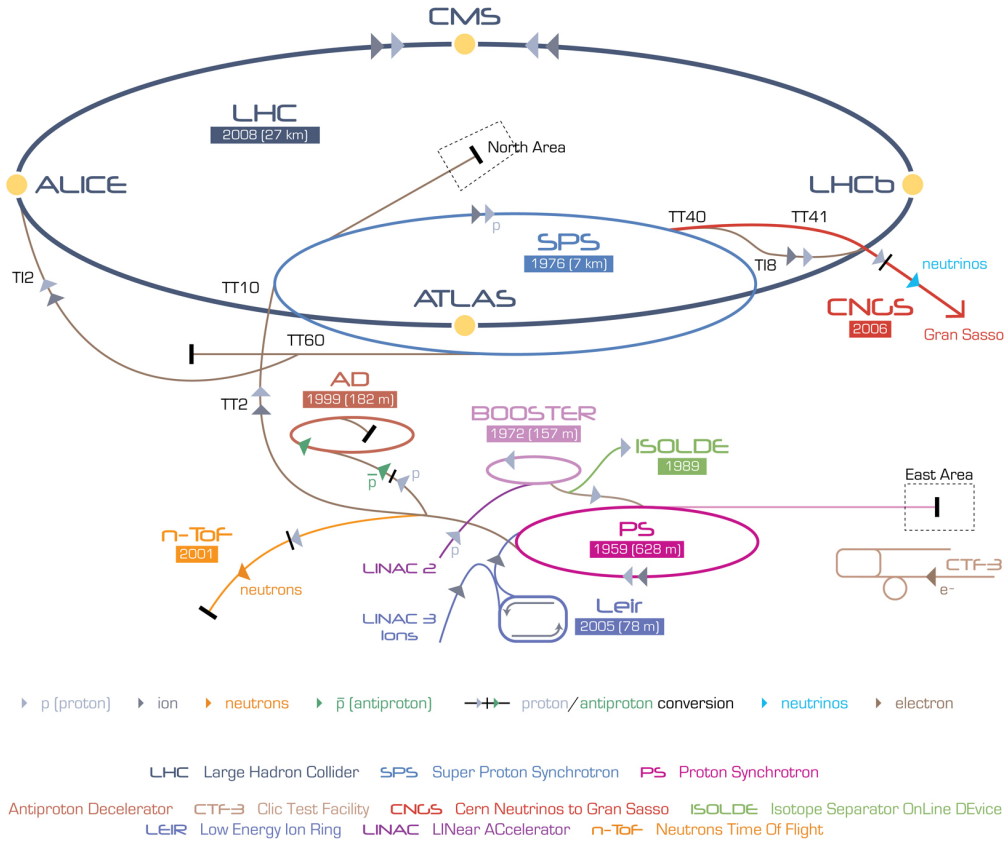
$$N_P = \sigma_P \int L. \quad (4.6)$$

585 Due to this simple relation, one can also quantify the “amount of data delivered” by
586 a collider simply by $\int L$.

587 4.2 Accelerator Complex

588 The Large Hadron Collider is the last accelerator in a chain of accelerators which
589 together form the CERN accelerator complex, which can be seen in 4.1. The protons

Figure 4.1: The CERN accelerator complex.



begin their journey to annihilation in a hydrogen source, where they are subsequently ionized. The first acceleration occurs in the Linac 2, a linear accelerator composed of RF cavities. The protons leave the Linac 2 at an energy of 50 MeV and enter the Proton Synchrotron Booster (PSB). The PSB contains four superimposed rings, which accelerate the protons to 1.4 GeV. The protons are then injected into the Proton Synchrotron (PS). This synchrotron increases the energy up to 25 GeV. After leaving the PS, the protons enter the Super Proton Synchrotron (SPS). This is the last step before entering the LHC ring, and the protons are accelerated to 450 GeV. From the SPS, the protons are injected into the beam pipes of the LHC. The process to fill the LHC rings with proton bunches from start to finish typically takes about four minutes.

601 4.3 Large Hadron Collider

The Large Hadron Collider is the final step in the CERN accelerator complex, and produces the collisions analyzed in this thesis. From the point of view of experimentalists on the general-purpose ATLAS and CMS experiments, the main goal of the LHC is to deliver collisions at the highest possible energy, with the highest possible instantaneous luminosity. The LHC was installed in the existing 27 km tunnel used by the Large Electron Positron (LEP) collider [87]. This allowed the existing accelerator complex at CERN, described in the previous section, to be used as the injection system to prepare the protons up to 450 GeV. Many aspects of the LHC design were decided by this very fact, and specified the options allowed to increase the energy or luminosity. In particular, the radius of the tunnel was already specified; from Eq.4.3, this implies the momentum (or energy) of the beam is entirely determined by the magnetic field. Given the 27 km circumference of the LEP tunnel, one can calculate the required magnetic field to reach the 7 TeV per proton design energy of the LHC :

$$r = C/2\pi = 4.3 \text{ km} \quad (4.7)$$

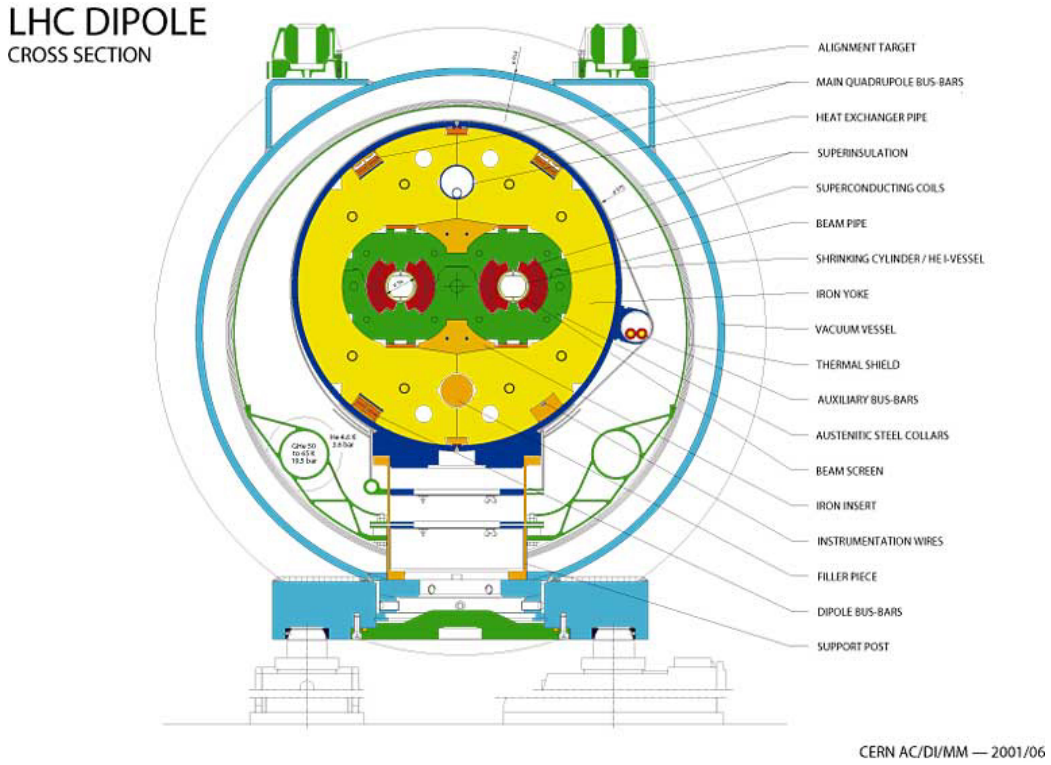
$$\rightarrow B = \frac{p}{rc} = 5 \text{ T} \quad (4.8)$$

602 In fact, the LHC consists of 8 528 m straight portions consisting of RF cavities, used
603 to accelerate the particles, and 8 circular portions which bend the protons around the
604 LHC ring. These circular portions actually have a slightly smaller radius of curvature
605 $r = 2804 \text{ m}$, and we require $B = 8.33 \text{ T}$. To produce this large field, we need to use
606 superconducting magnets, as discussed in the next section.

607 Magnets

608 There are many magnets used by the LHC machine, but the most important are the
609 1232 dipole magnets; a schematic is shown in Fig.4.2 and a photograph is shown in

Figure 4.2: Schematic of an LHC dipole magnet.



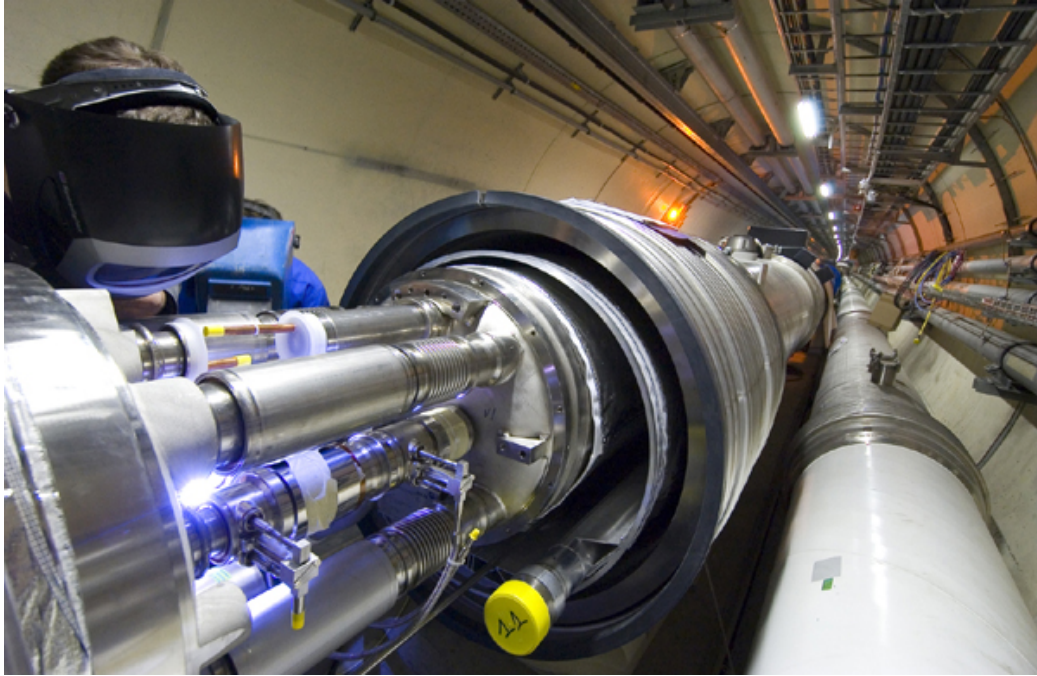
610 Fig.4.3.

611 The magnets are made of Niobium and Titanium. The maximum field strength is
 612 10 T when cooled to 1.9 Kelvin. The magnets are cooled by superfluid helium, which
 613 is supplied by a large cryogenic system. Due to heating between the eight helium
 614 refrigerators and the beampipe, the helium is cooled in the refrigerators to 1.8 K.

615 A failure in the cooling system can cause what is known as a *quench*. If the
 616 temperature goes above the critical superconducting temperature, the metal loses its
 617 superconducting properties, which leads to a large resistance in the metal. This leads
 618 to rapid temperature increases, and can cause extensive damages if not controlled.

619 The dipole magnets are 16.5 meters long with a diameter of 0.57 meters. There
 620 are two individual beam pipes inside each magnet, which allows the dipoles to house
 621 the beams travelling in both directions around the LHC ring. They curve slightly,
 622 at an angle of 5.1 mrad, which carefully matches the curvature of the ring. The

Figure 4.3: Photograph of a technician connecting an LHC dipole magnet.



623 beampipes inside of the magnets are held in high vacuum, to avoid stray particles
624 interacting with the beam.

625 **4.4 Dataset Delivered by the LHC**

626 In this thesis, we analyze the data delivered by the LHC to ATLAS in the 2015 and
627 2016 datasets. The beam parameters relevant to this dataset are available in Table
628 [4.1](#).

629 The peak instantaneous luminosity delivered in 2015 (2016) was $L =$
630 $5.2(11) \text{ cm}^{-2}\text{s}^{-1} \times 10^{33}$. One can note that the instantaneous luminosity delivered in
631 the 2016 dataset exceeds the design luminosity of the LHC. The total integrated
632 luminosity delivered was 13.3 fb^{-1} . In Figure [4.4](#), we display the integrated luminosity
633 as a function of day for 2015 and 2016.

Figure 4.4: Integrated Luminosity delivered by the LHC and collected by ATLAS in the 2015 and 2016 datasets.

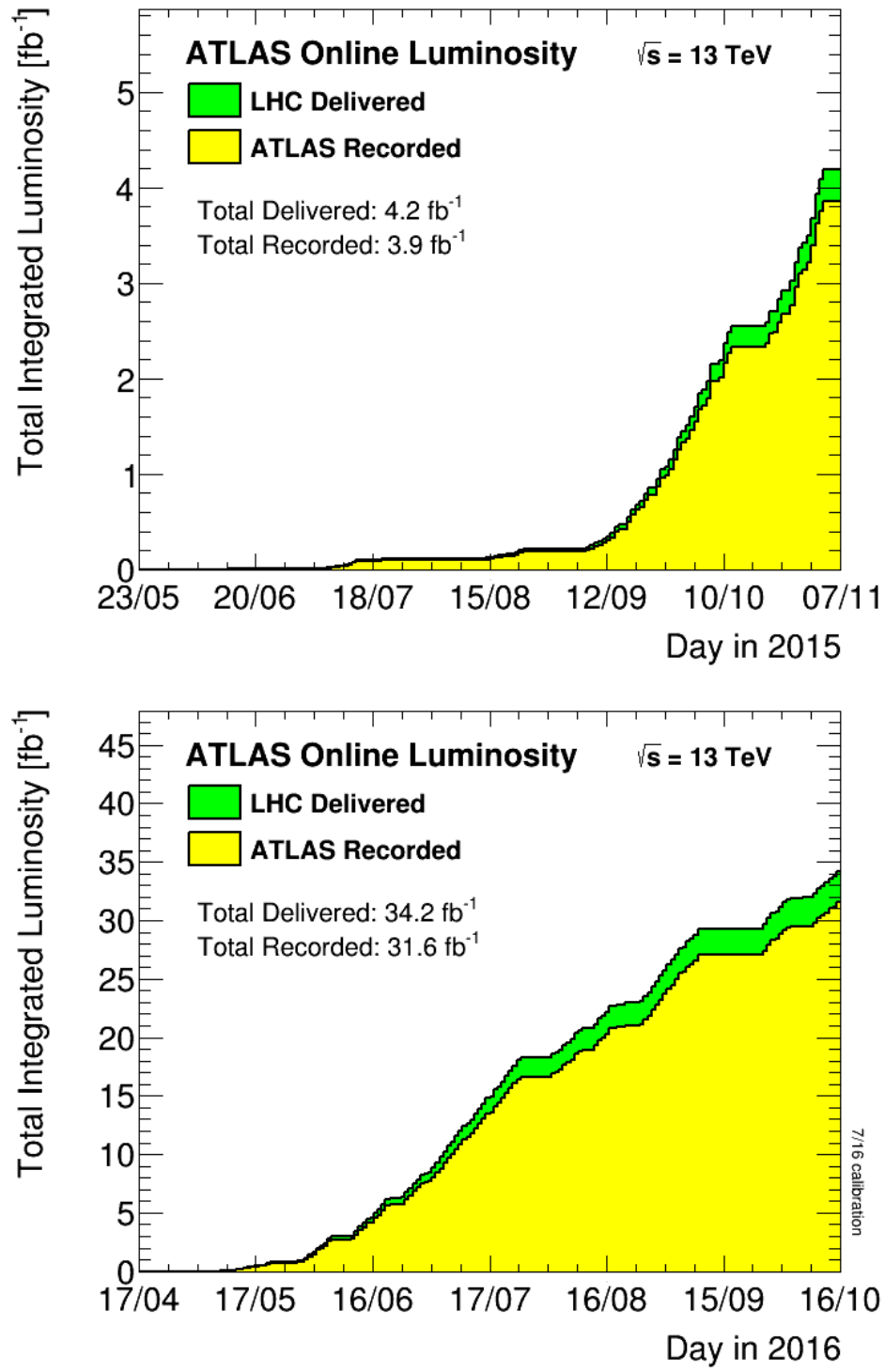
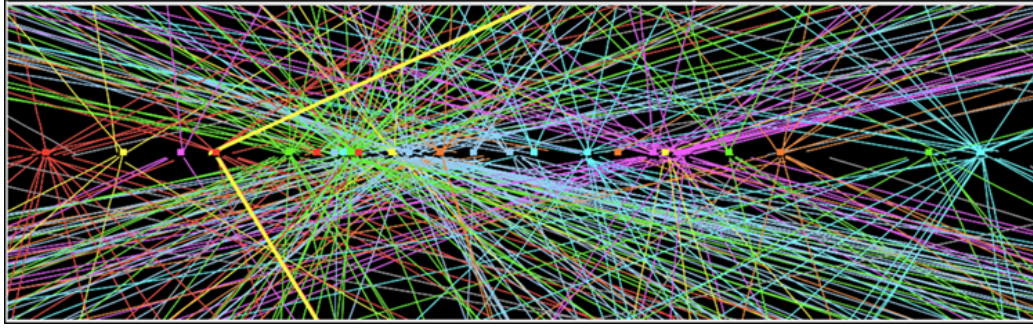


Table 4.1: Beam parameters of the Large Hadron Collider.

Parameter	Injection	Extraction
Energy (GeV)	450	7000
Rigidity (T-m)	3.8	23353
Bunch spacing (ns)	25	25
Design Luminosity ($\text{cm}^{-2}\text{s}^{-1} \times 10^{34}$)	-	1.0
Bunches per proton beam	2808	2808
Protons per bunch	1.15 e11	1.15 e11
Beam lifetime (hr)	-	10
Normalized Emittance ϵ_N (mm μrad)	3.3	3.75
Betatron function at collision point β^* (cm)	-	55

Figure 4.5: Simulated event with many pileup vertices.



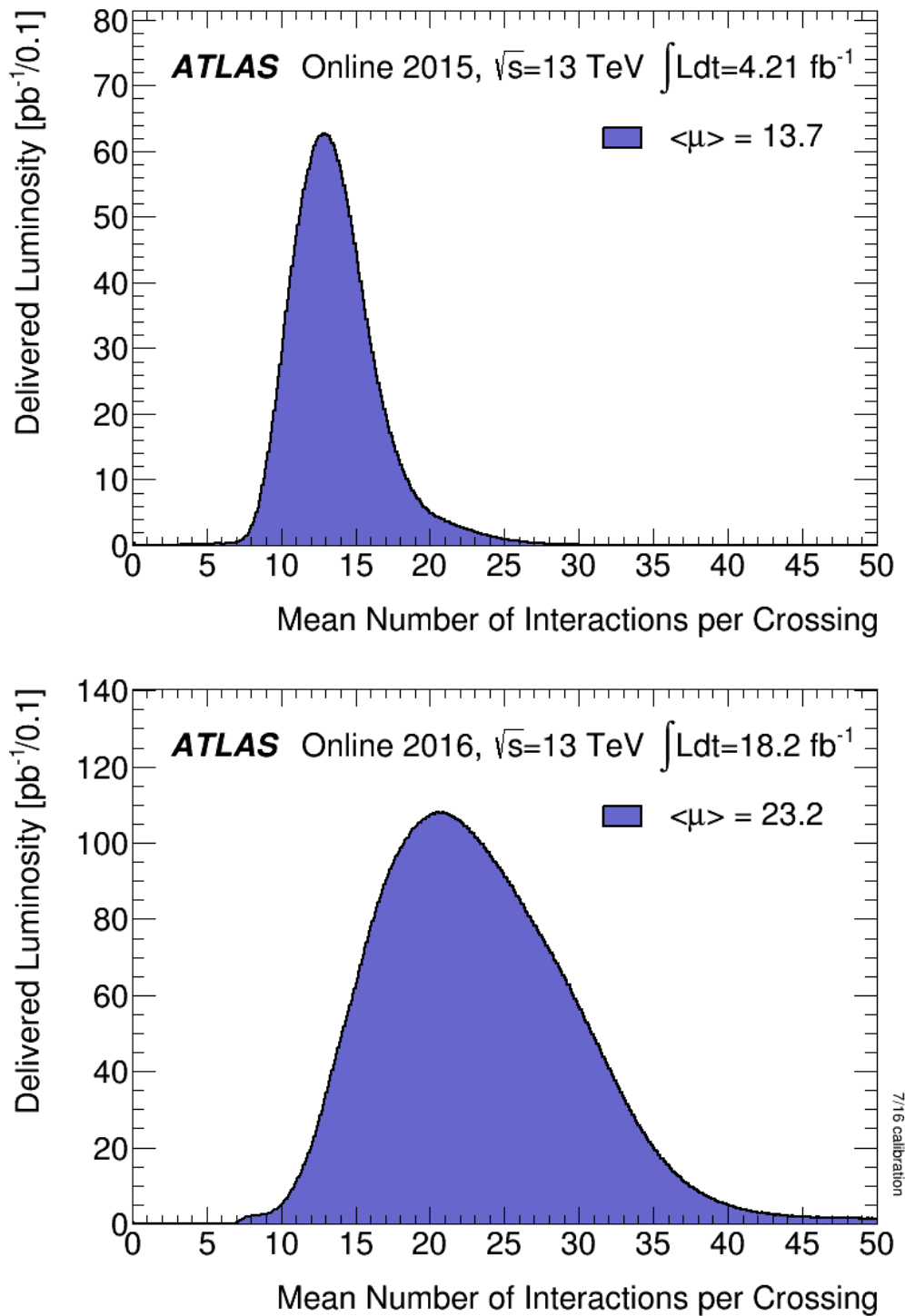
634 Pileup

635 *Pileup* is the term for the additional proton-proton interactions which occur during
 636 each bunch crossing of the LHC. At the beginning of the LHC physics program, there
 637 had not been a collider which averaged more than a single interaction per bunch
 638 crossing. In the LHC, each bunch crossing (or *event*) generally contains multiple
 639 proton-proton interactions. An simulated event with many *vertices* can be seen in
 640 Fig.4.5 The so-called *primary vertex* (or *hard scatter vertex*) refers to the vertex which
 641 has the highest Σp_T^2 ; this summation occurs over the *tracks* in the detector, which
 642 we will describe later. We then distinguish between *in-time* pileup and *out-of-time*
 643 pileup. In-time pileup refers to the additional proton-proton interactions which occur
 644 in the event. Out-of-time pileup refers to effects related to proton-proton interactions
 645 previous bunch crossings.

646 We quantify in-time pileup by the number of “primary”² vertices in a particular
647 event. To quantify the out-of-time pileup, we use the average number of interactions
648 per bunch crossing $\langle \mu \rangle$ over some human-scale time. In Figure 4.6, we show the
649 distribution of μ for the dataset used in this thesis.

²The primary vertex is as defined above, but we unfortunately use the same name here.

Figure 4.6: Mean number of interactions per bunch crossing in the 2015 and 2016 datasets.



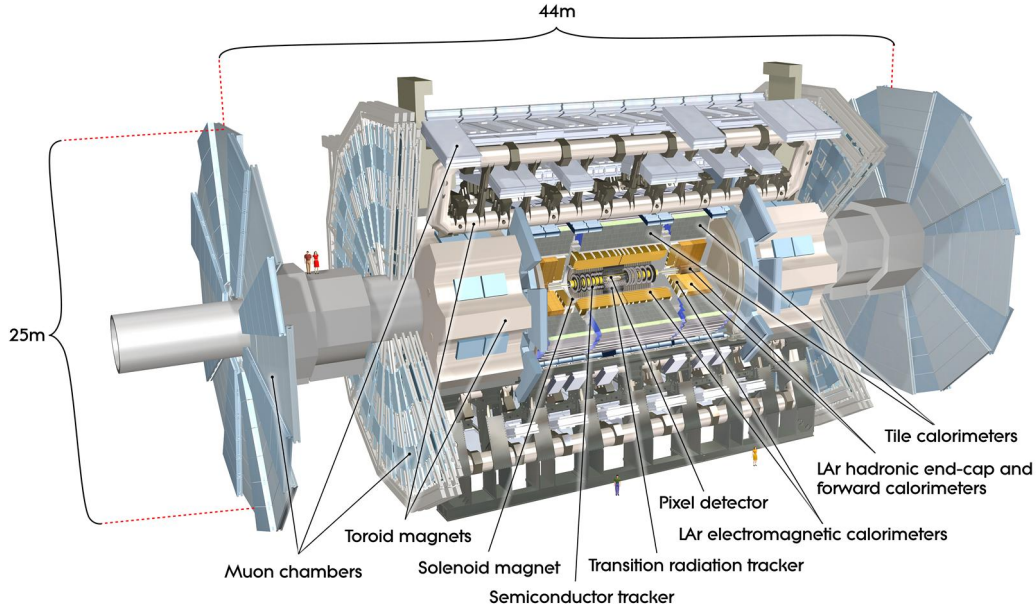
The ATLAS detector

652 The dataset analyzed in this thesis was taken by the ATLAS detector [88], which is
 653 located at the “Point 1” cavern of the LHC beampipe, just across the street from
 654 the main CERN campus. The much-maligned acronym stands for *A Toroidal LHC*
 655 *ApparatuS*. ATLAS is a massive cylindrical detector, with a radius of 12.5 m and a
 656 length of 44 m, with nearly hermitic coverage around the collision point. It consists
 657 of multiple subdetectors; each plays a role in ATLAS’s ultimate purpose of measuring
 658 the energy, momentum, and type of the particles produced in collisions delivered by
 659 the LHC. These subdetectors are immersed in a hybrid solenoid-toroid magnet system
 660 whichs forces charged particles to curve, which allows for precise measurements of
 661 their momenta. These magnetic fields are maximized in the central solenoid magnet,
 662 which contains a magnetic field of 2 T. A schematic of the detector can be seen in
 663 [5.1](#).

664 The *inner detector* (ID) lies closest to the collision point, and contains three
 665 separate subdetectors. It provides pseudorapidity¹coverage of $|\eta| < 2.5$ for charged
 666 particles to interact with the tracking material. The tracks reconstructed from the
 667 inner detector hits are used to reconstruct the primary vertices, as noted in Ch.??,

¹ATLAS uses a right-handed Cartesian coordinate system; the origin is defined by the nominal beam interaction point. The positive- z direction is defined by the incoming beam travelling counterclockwise around the LHC. The positive- x direction points towards the center of the LHC ring from the origin, and the positive- y direction points upwards towards the sky. For particles of transverse (in the $x - y$ plane) momentum $p_T = \sqrt{p_x^2 + p_y^2}$ and energy E , it is generally most convenient fully describe this particle’s kinematics as measured by the detector in the (p_T, ϕ, η, E) basis. The angle $\phi = \arctan(p_y/p_x)$ is the standard azimuthal angle, and $\eta = \ln \tan(\theta/2)$ is known as the pseudorapidity, and defined based on the standard polar angle $\theta = \arccos(p_z/p_T)$. For locations of i.e. detector elements, both (r, ϕ, η) and (z, ϕ, η) can be useful.

Figure 5.1: The ATLAS detector

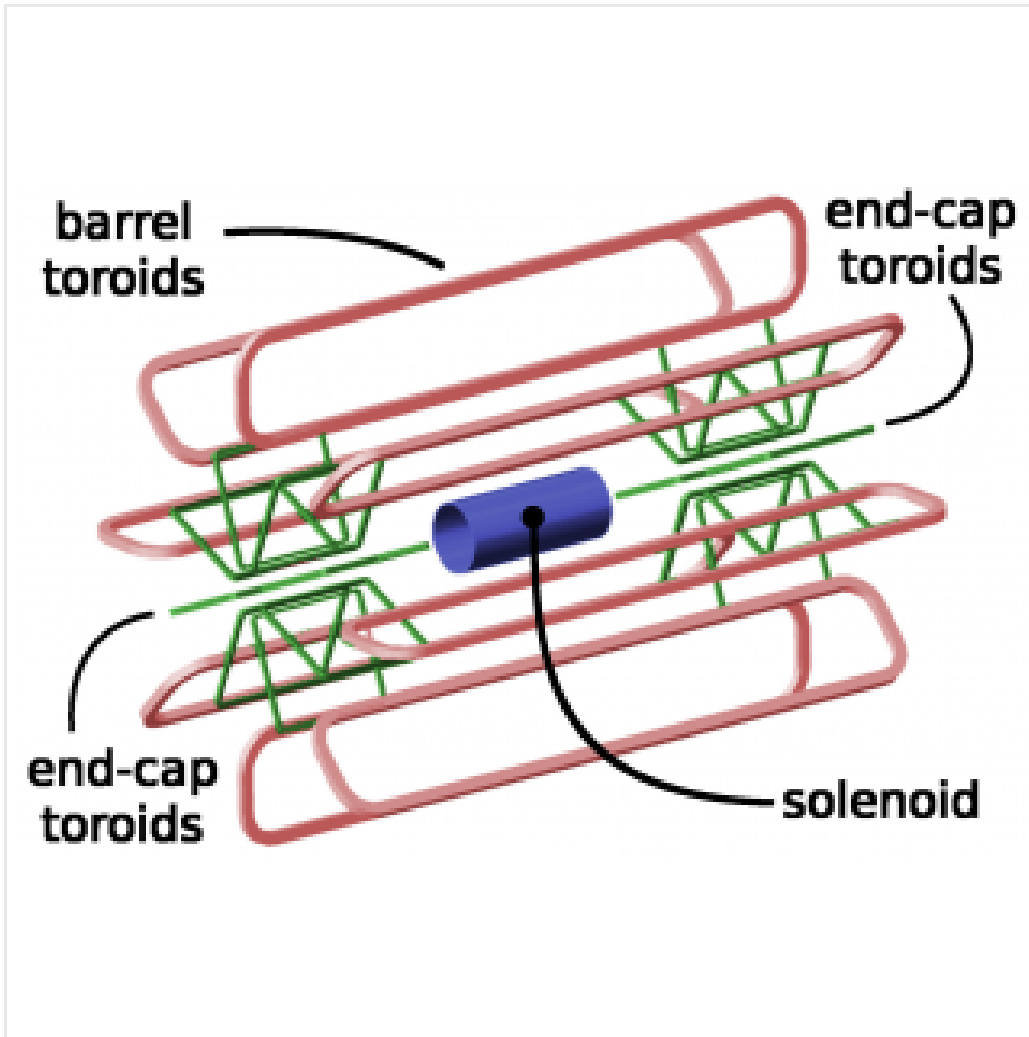


and to determine the momenta of charged particles. The ATLAS *calorimeter* consists of two subdetectors, known as the *electromagnetic* and *hadronic* calorimeters. These detectors stop particles in their detector material, and measure the energy deposition inside, which measures the energy of the particles deposited. The calorimeters provide coverage out to pseudorapidity of $|\eta| < 4.9$. The muon spectrometer is aptly named; it is specifically used for muons, which are the only particles which generally reach the outer portions of the detector. In this region, we have the large tracking systems of the muon spectrometer, which provide precise measurements of muon momenta. The muon spectrometer has pseudorapidity coverage of $|\eta| < 2.7$.

5.1 Magnets

ATLAS contains multiple magnetic systems; primarily, we are concerned with the solenoid, used by the inner detector, and the toroids located outside of the ATLAS calorimeter. A schematic is shown in Fig.5.2. These magnetic fields are used to bend

Figure 5.2: The ATLAS magnet system

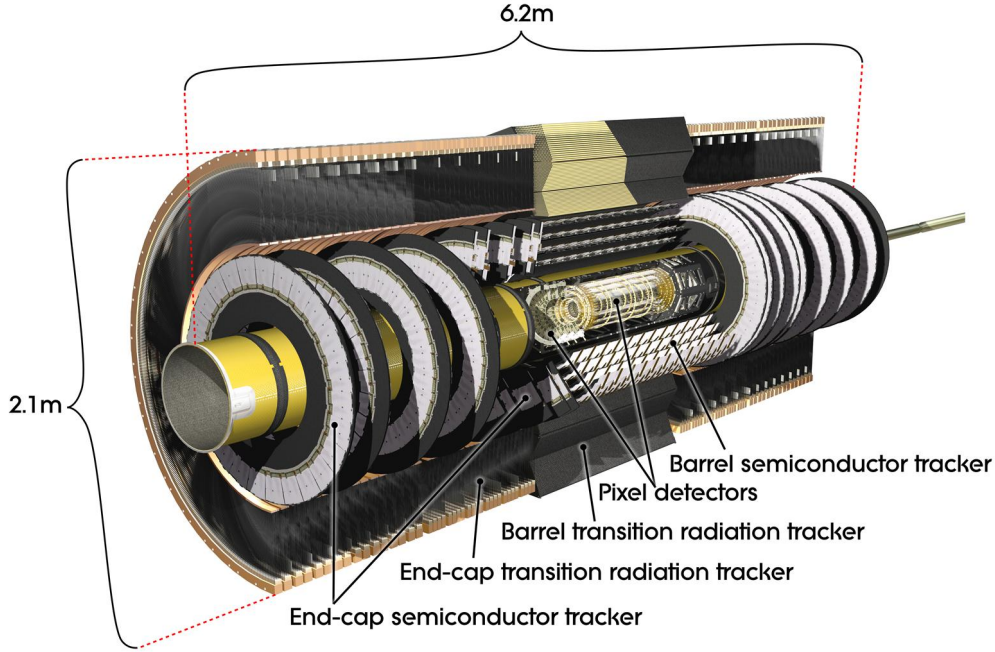


681 charged particles under the Lorentz force, which subsequently allows one to measure
682 their momentum.

683 The ATLAS central solenoid is a 2.3 m diameter, 5.3 m long solenoid at the center
684 of the ATLAS detector. It produces a uniform magnetic field of 2 T; this strong field
685 is necessary to accurately measure the charged particles in this field. An important
686 design constraint for the central solenoid was the decision to place it in between the
687 inner detector and the calorimeters. To avoid excessive impacts on measurements in
688 the calorimetry, the central solenoid must be as transparent as possible².

²This is also one of the biggest functional differences between ATLAS and CMS; in CMS, the

Figure 5.3: The ATLAS inner detector



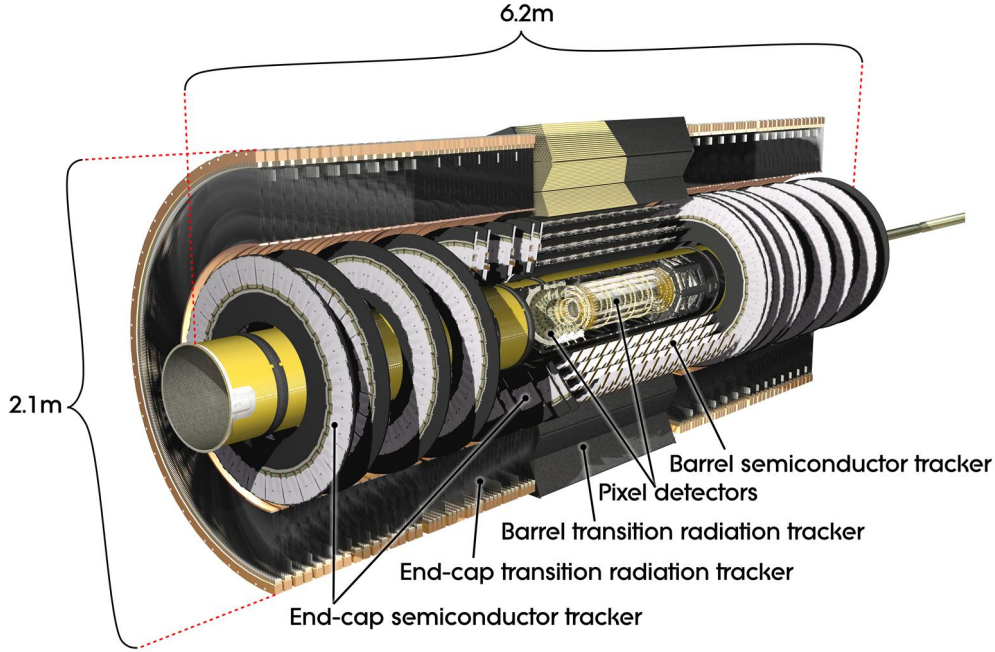
689 The toroid system consists of eight air-core superconducting barrel loops; these
690 give ATLAS its distinctive shape. There are also two endcap air-core magnets. These
691 produce a magnetic field in a region of approximately 26 m in length and 10 m of
692 radius. The magnetic field in this region is non-uniform, due to the prohibitive costs
693 of a solenoid magnet of that size.

694 **5.2 Inner Detector**

695 The ATLAS inner detector consists of three separate tracking detectors, which are
696 known as, in order of increasing distance from the interaction point, the Pixel
697 Detector, Semiconductor Tracker (SCT), and the Transition Radiation Tracker
698 (TRT). When charged particles pass through these tracking layers, they produce
699 *hits*, which using the known 2 T magnetic field, allows the reconstruction of *tracks*.
700 Tracks are used as inputs for reconstruction of many higher-level physics objects,

solenoid is outside of the calorimeters.

Figure 5.4: The ATLAS pixel detector



701 such as electrons, muons, photons, and E_T^{miss} . Accurate track reconstruction is thus
702 crucial for precise measurements of charged particles.

703 Pixel Detector

704 The ATLAS pixel detector consists four layers of silicon “pixels”. This refers to the
705 segmentation of the active medium into the pixels; compare to the succeeding silicon
706 detectors, which will use silicon “strips”. This provides precise 3D hit locations. The
707 layers are known as the “Insertable”³B-Layer (IBL), the B-Layer (or Layer-0), Layer-
708 1, and Layer-2, in order of increasing distance from the interaction point. These
709 layers are very close to the interaction point, and therefore experience a large amount
710 of radiation.

711 Layer-1, Layer-2, and Layer-3 were installed with the initial construction of
712 ATLAS. They contain front-end integrated electronics (FEI3s) bump-bonded to 1744

³Very often, the IBL is mistakenly called the Inner B-Layer, which would have been a much more sensible name.

713 silicon modules; each module is $250\ \mu\text{m}$ in thickness and contains 47232 pixels. These
714 pixels have planar sizes of $50 \times 400\ \mu^2$ or $50 \times 600\ \mu^2$, to provide highly accurate
715 location information. The FEI3s are mounted on long rectangular structures known
716 as staves, which encircle the beam pipe. A small tilt to each stave allows full coverage
717 in ϕ even with readout systems which are installed. These layers are at radia of 50.5
718 mm, 88.5 mm, and 122.5 mm from the interaction point.

719 The IBL was added to ATLAS after Run1 in 2012 at a radius of 33 mm from the
720 interaction point. The entire pixel detector was removed from the center of ATLAS
721 to allow an additional pixel layer to be installed. The IBL was required to preserve
722 the integrity of the pixel detector as radiation damage leads to inoperative pixels in
723 the other layers. The IBL consists of 448 FEI4 chips, arranged onto 14 staves. Each
724 FEI4 has 26880 pixels, of planar size $50 \times 250\ \mu\text{m}$. This smaller granularity was
725 required due to the smaller distance to the interaction point.

726 In total, a charged particle passing through the inner detector would expect to
727 leave four hits in the pixel detector.

728 Semiconductor Tracker

729 The SCT is directly beyond Layer-2 of the pixel detector. This is a silicon strip
730 detector, which do not provide the full 3D information of the pixel detector. The
731 dual-sensors of the SCT contain 2×768 individual strips; each strip has area $6.4\ \text{cm}^2$.
732 The SCT dual-sensor is then double-layered, at a relative angle of 40 mrad;
733 together these layers provide the necessary 3D information for track reconstruction.
734 There are four of these double-layers, at radia of 284 mm, 355 mm, 427 mm, and 498
735 mm. These double-layers provide hits comparable to those of the pixel detector, and
736 we have four additional hits to reconstruct tracks for each charged particle.

Figure 5.5: A ring of the Semiconductor Tracker

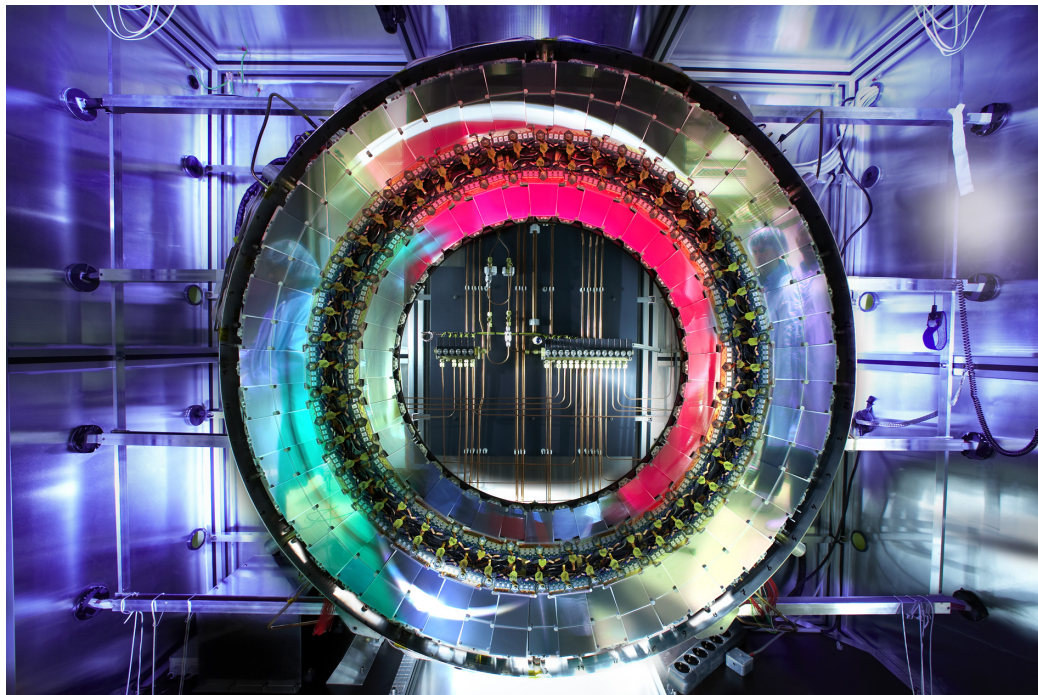
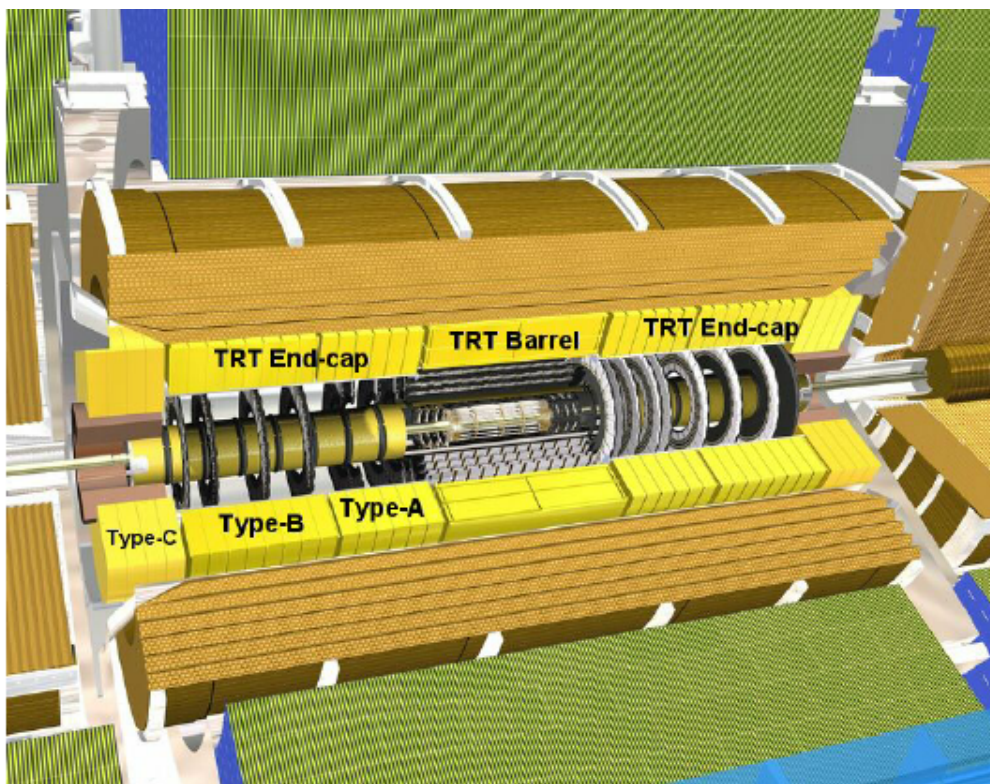


Figure 5.6: A schematic of the Transition Radiation Tracker



737 **Transition Radiation Tracker**

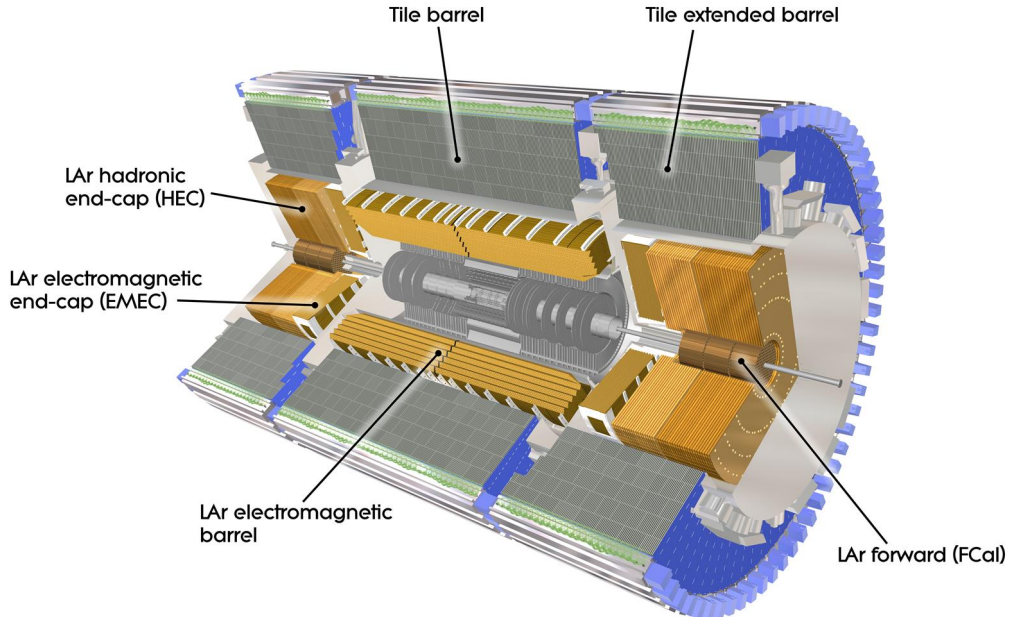
738 The Transition Radiation Tracker is the next detector radially outward from the SCT.
739 It contains straw drift tubes; these contain a tungsten gold-plated wire of $32\ \mu\text{m}$
740 diameter held under high voltage (-1530 V) with the edge of the Kapton-aluminum
741 tube. They are filled with a gas mixture of primarily xenon that is ionized when
742 a charged particle passes through the tube. The ions are collected by the “drift”
743 due to the voltage inside the tubes, which is read out by the electronics. This gives
744 so-called “continuous tracking” throughout the tube, due to the large number of ions
745 produced.

746 The TRT is so-named due to the *transition radiation* (TR) it induces. Due to
747 the dielectric difference between the gas and tubes, TR is induced. This is important
748 for distinguishing electrons from their predominant background of minimum ionizing
749 particles. Generally, electrons have a much larger Lorentz factor than minimum
750 ionizing particles, which leads to additional TR. This can be used as an additional
751 handle for electron reconstruction.

752 **5.3 Calorimetry**

753 The calorimetry of the ATLAS detector also includes multiple subdetectors; these sub-
754 detectors allow precise measurements of the electrons, photons, and hadrons produced
755 by the ATLAS detector. Generically, calorimeters work by stopping particles in their
756 material, and measuring the energy deposition. This energy is deposited as a cascade
757 particles induce from interactions with the detector material known *showers*. ATLAS
758 uses *sampling* calorimeters; these alternate a dense absorbing material, which induces
759 showers, with an active layer which measures energy depositions by the induced
760 showers. Since some energy is deposited into the absorption layers as well, the energy
761 depositions must be properly calibrated for the detector.

Figure 5.7: The ATLAS calorimeter

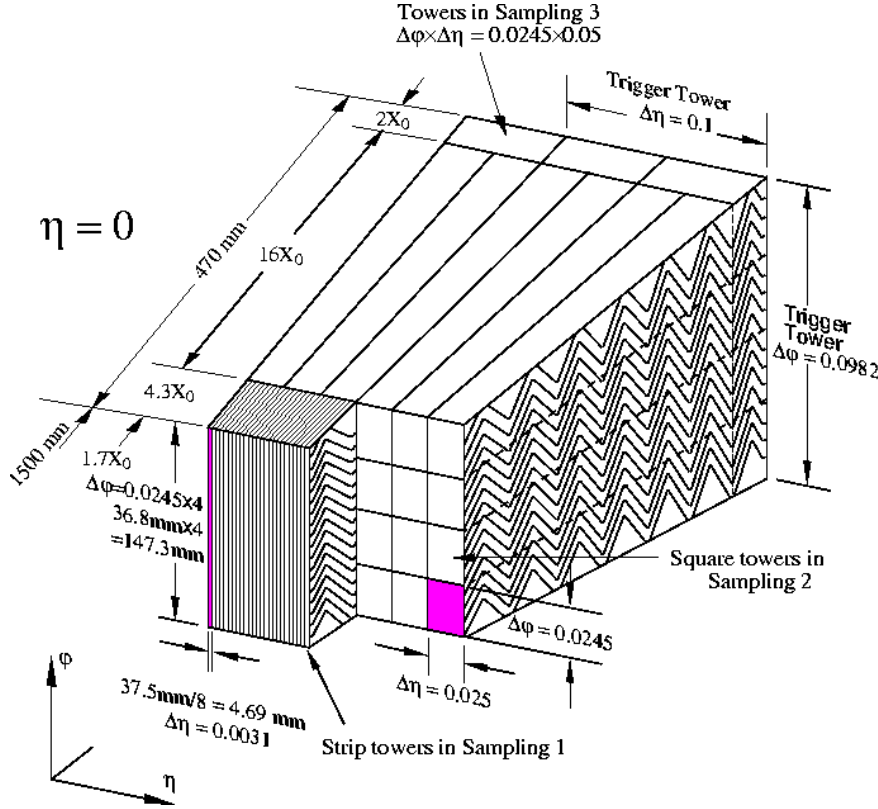


762 Electromagnetic objects (electrons and photons) and hadrons have much different
 763 interaction properties, and thus we need different calorimeters to accurately measure
 764 these different classes of objects; we can speak of the *electromagnetic* and *hadronic*
 765 calorimeters. ATLAS contains four separate calorimeters : the liquid argon (LAr)
 766 electromagnetic barrel calorimeter, the Tile barrel hadronic calorimeter, the LAr
 767 endcap electromagnetic calorimeter, the LAr endcap hadronic calorimeter, and the
 768 LAr Forward Calorimeter (FCal). Combined, these provide full coverage in ϕ up to
 769 $|\eta| < 4.9$, and can be seen in Fig.5.7.

770 Electromagnetic Calorimeters

771 The electromagnetic calorimeters of the ATLAS detector consist of the barrel and
 772 endcap LAr calorimeters. These are arranged into an ingenious “accordion” shape,
 773 shown in 5.8, which allows full coverage in ϕ and exceptional coverage in η while
 774 still allowing support structures for detector operation. The accordion is made of

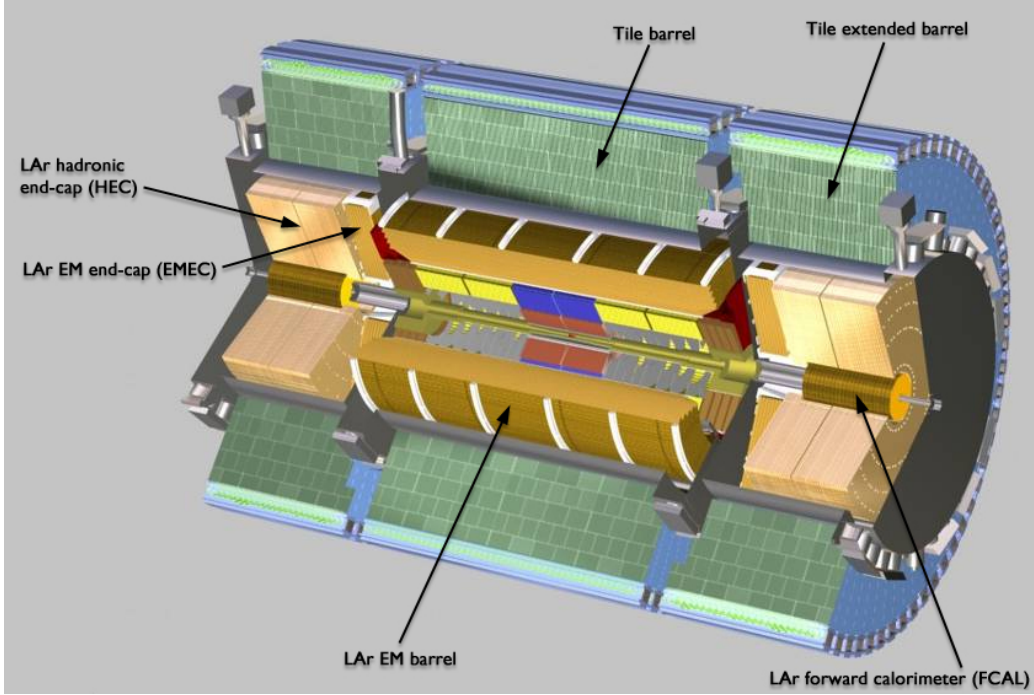
Figure 5.8: A schematic of a subsection of the barrel LAr electromagnetic calorimeter



775 layers with liquid argon (active detection material) and lead (absorber) to induce
 776 electromagnetic showers. The LAr EM calorimeters are each more than 20 radiation
 777 lengths deep, which provides the high stopping power necessary to properly measure
 778 the electromagnetic showers.

779 The barrel component of the LAr EM calorimeter extends from the center of the
 780 detector out to $|\eta| < 1.475$. The calorimeter has a presampler, which measures the
 781 energy of any EM shower induced before the calorimeter. This has segmentation of
 782 $\Delta\eta = 0.025, \Delta\phi = .01$. There are three “standard” layers in the barrel, which have
 783 decreasing segmentation into calorimeter *cells* as one travels radially outward from
 784 the interaction point. The first layer has segmentation of $\Delta\eta = 0.003, \Delta\phi = .1$, and
 785 is quite thin relative to the other layers at only 4 radiation lengths deep. It provides
 786 precise η and ϕ measurements for incoming EM objects. The second layer is the
 787 deepest at 16 radiation lengths, with a segmentation of $\Delta\eta = 0.025, \Delta\phi = 0.025$. It

Figure 5.9: A schematic of Tile hadronic calorimeter



is primarily responsible for stopping the incoming EM particles, which dictates its large relative thickness, and measures most of the energy of the incoming particles. The third layer is only 2 radiation lengths deep, with a rough segmentation of $\Delta\eta = 0.05$, $\Delta\phi = .025$. The deposition in this layer is primarily used to distinguish hadrons interacting electromagnetically and entering the hadronic calorimeter from the strictly EM objects which are stopped in the second layer.

The barrel EM calorimeter has a similar overall structure, but extends from $1.4 < |\eta| < 3.2$. The segmentation in η is better in the endcap than the barrel; the ϕ segmentation is the same. In total, the EM calorimeters contain about 190000 individual calorimeter cells.

Hadronic Calorimeters

The hadronic calorimetry of ATLAS sits directly outside the EM calorimetry. It contains three subdetectors : the barrel Tile calorimeter, the endcap LAr calorimeter,

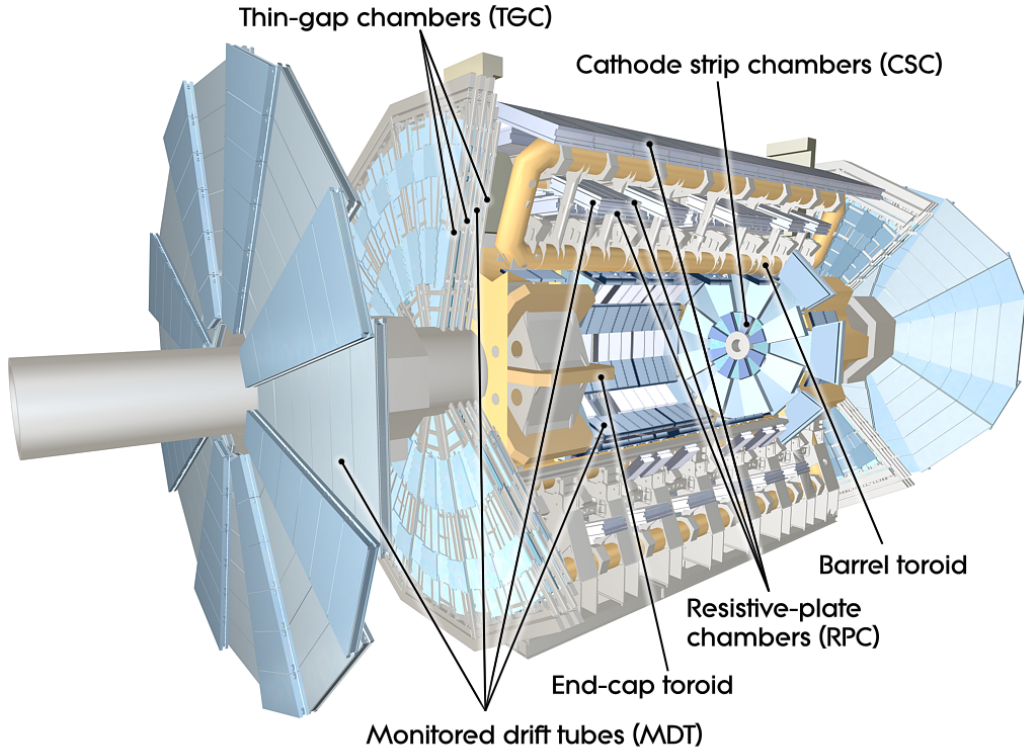
801 and the Forward LAr Calorimeter. Similar to the EM calorimeters, these are
802 sampling calorimeters that alternate steel (dense material) with an active layer
803 (plastic scintillator).

804 The barrel Tile calorimeter extends out to $|\eta| < 1.7$. There are again three layers,
805 which combined give about 10 interactions length of distance, which provides excellent
806 stopping power for hadrons. This is critical to avoid excess *punchthrough* to the muon
807 spectrometer beyond the hadronic calorimeters. The first layer has a depth of 1.5
808 interaction lengths. The second layer is again the thickest at a depth of 4.1 interaction
809 lengths; most of the energy of incoming particle is deposited here. Both the first and
810 second layer have segmentation of about $\Delta\eta = 0.1, \Delta\phi = 0.1$. Generally, one does not
811 need as fine of granularity in the hadronic calorimeter, since the energy depositions
812 in the hadronic calorimeters will be summed into the composite objects we know as
813 jets. The third layer has a thickness of 1.8 interaction lengths, with a segmentation of
814 $\Delta\eta = 0.2, \Delta\phi = 0.1$. The use of multiple layers allows one to understand the induced
815 hadronic shower as it propagates through the detector material.

816 The endcap LAr hadronic calorimeter covers the region $1.5 < |\eta| < 3.2$. It is
817 again a sampling calorimeter; the active material is LAr with a copper absorbed. It
818 does not use the accordion shape of the other calorimeters; it has a “standard” flat
819 shape perpendicular to the interaction point. The segmentation varies with η . For
820 $1.5 < |\eta| < 2.5$, the cells are $\Delta\eta = 0.1, \Delta\phi = 0.1$; in the region $2.5 < |\eta| < 3.2$, the
821 cells are $\Delta\eta = 0.2, \Delta\phi = 0.2$ in size.

822 The final calorimeter in ATLAS is the forward LAr calorimeter. Of those
823 subdetectors which are used for standard reconstruction techniques, the FCal sits
824 at the most extreme values of $3.1 < |\eta| < 4.9$. The FCal itself is made of three
825 subdetectors; FCal1 is actually an electromagnetic module, while FCal2 and FCal3
826 are hadronic. The absorber in FCal1 is copper, with a liquid argon active medium.
827 FCal2 and FCal3 also use a liquid argon active medium, with a tungsten absorber.

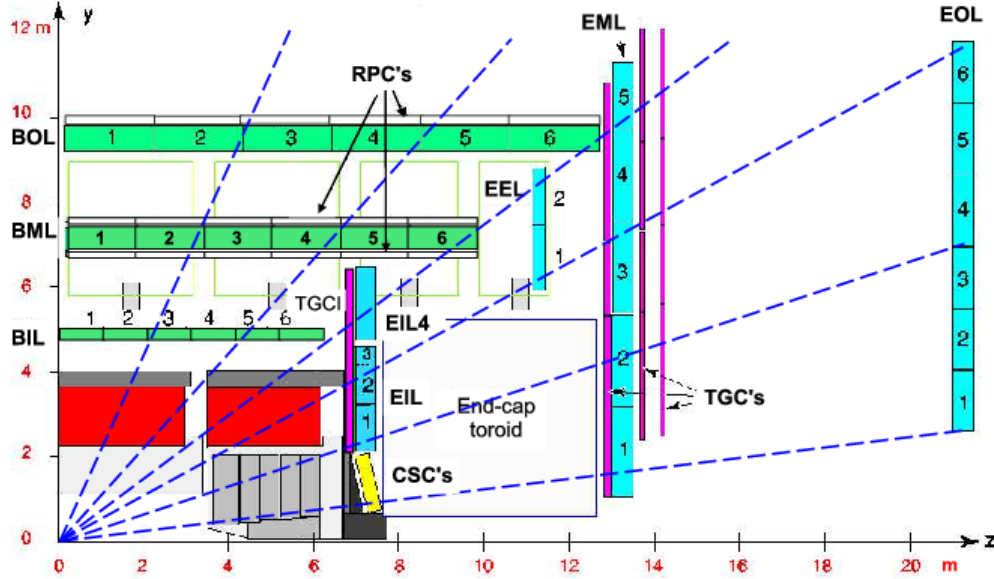
Figure 5.10: The ATLAS muon spectrometer



828 5.4 Muon Spectrometer

829 The muon spectrometer is the final major subdetector of the ATLAS detector.
830 The muon spectrometer sits outside the hadronic calorimetry, with pseudorapidity
831 coverage out to $|\eta| < 2.7$. The MS is a huge detector, with some detector elements
832 existing as far as 11 m in radius from the interaction point. This system is used
833 almost exclusively to measure the momenta of muons; these are the only measured
834 SM particles which consistently exit the hadronic calorimeters. These systems provide
835 a rough measurement, which is used in triggering (described in Ch.5.5), and a precise
836 measurement to be used in offline event reconstruction as described in Ch.???. The
837 MS produces tracks in a similar way to the ID; the hits in each subdetector are
838 recorded and then tracks are produced from these hits. Muon spectrometer tracks are
839 largely independent of the ID tracks due to the independent solenoidal and toroidal
840 magnet systems used in the ID and MS respectively. The MS consists of four separate

Figure 5.11: A schematic in z/η showing the location of the subdetectors of the muon spectrometer

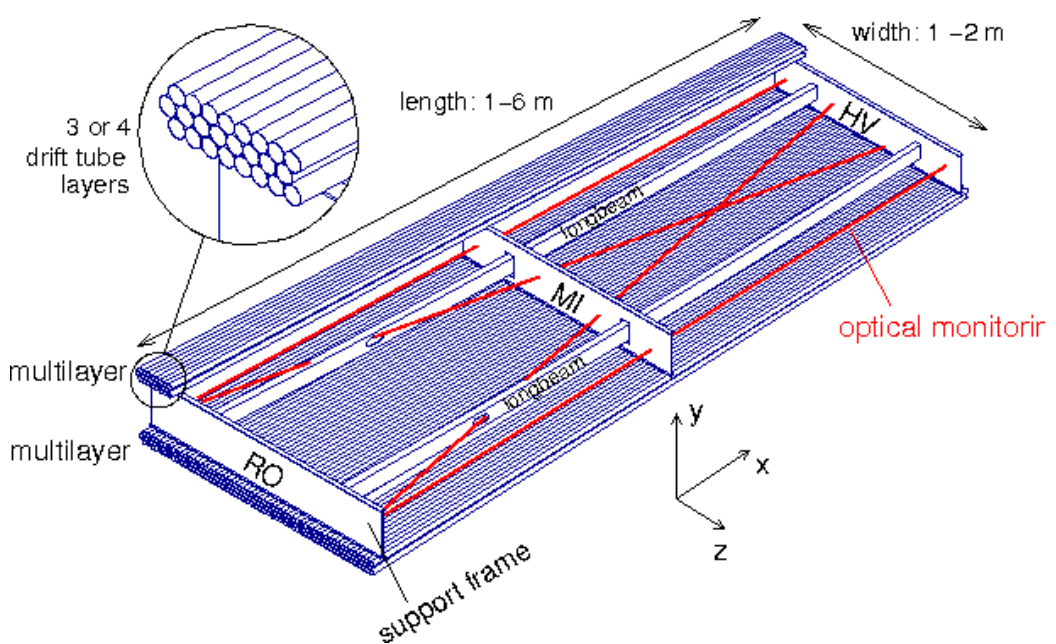


841 subdetectors: the barrel region is covered by the Resistive Plate Chambers (RPCs)
 842 and Monitored Drift Tubes (MDTs) while the endcaps are covered by MDTs, Thin
 843 Gap Chambers (TGCs), and Cathode Strip Chambers (CSCs).

844 Monitored Drift Tubes

845 The MDT system is the largest individual subdetector of the MS. MDTs provide
 846 precision measurements of muon momenta as well as fast measurements used for
 847 triggers. There are 1088 MDT chambers providing coverage out to pseudorapidity
 848 $|\eta| < 2.7$; each consists of an aluminum tube containing an argon- CO_2 gas mixture.
 849 In the center of each tube there $50\mu\text{m}$ diameter tungsten-rhenium wire at a voltage of
 850 3080 V. A muon entering the tube will induce ionization in the gas, which will “drift”
 851 towards the wire due to the voltage. One measures this ionization as a current in the
 852 wire; this current comes with a time measurement related to how long it takes the
 853 ionization to drift to the wire.

Figure 5.12: Schematic of a Muon Drift Tube chamber



854 These tubes are layered in a pattern shown in Fig.5.12. Combining the measure-
855 ments from the tubes in each layer gives good position resolution. The system consists
856 of three subsystems of these layers, at 5 m, 7m, and 9 m from the interaction point.
857 The innermost layer is directly outside the hadronic calorimeter. The combination of
858 these three measurements gives precise momenta measurements for muons.

859 **Resistive Plate Chambers**

860 The RPC system is alternated with the MDT system in the barrel; the first two layers
861 of RPC detectors surround the second MDT layer while the third is outside the final
862 MDT layer. The RPC system covers pseudorapidity $|\eta| < 1.05$. Each RPC consists
863 of two parallel plates at a distance of 2 mm surrounding a $\text{C}_2\text{H}_2\text{F}_4$ mixture. The
864 electric field between these plates is 4.9k kV/mm. Just as in the MDTs, an incoming
865 muon ionizes the gas, and the deposited ionization is collected by the detector (in this
866 case on the plates). It is quite fast, but with a relatively poor spatial resolution of
867 1 cm. Still, it can provide reasonable ϕ resolution due to its large distance from the
868 interaction point. This is most useful in triggering, where the timing requirements are
869 quite severe. The RPCs are also complement the MDTs by providing a measurement
870 of the non-bending coordinate.

871 **Cathode Strip Chambers**

872 The CSCs are used in place of MDTs in the first layer of the endcaps. This region, at
873 $2.0 < |\eta| < 2.7$, has higher particle multiplicity at the close distance to the interaction
874 point from low-energy photons and neutrons. The MDTs were not equip to deal with
875 the higher particle rate of this region, so the CSCs were designed to deal with this
876 deficiency.

877 Each CSC consists multiwire proportional chambers, oriented radially outward
878 from the interaction point. These chambers overlap partially in ϕ . The wires contain

Figure 5.13: Photo of the installation of Cathode Strip Chambers and Monitored Drift Tubes



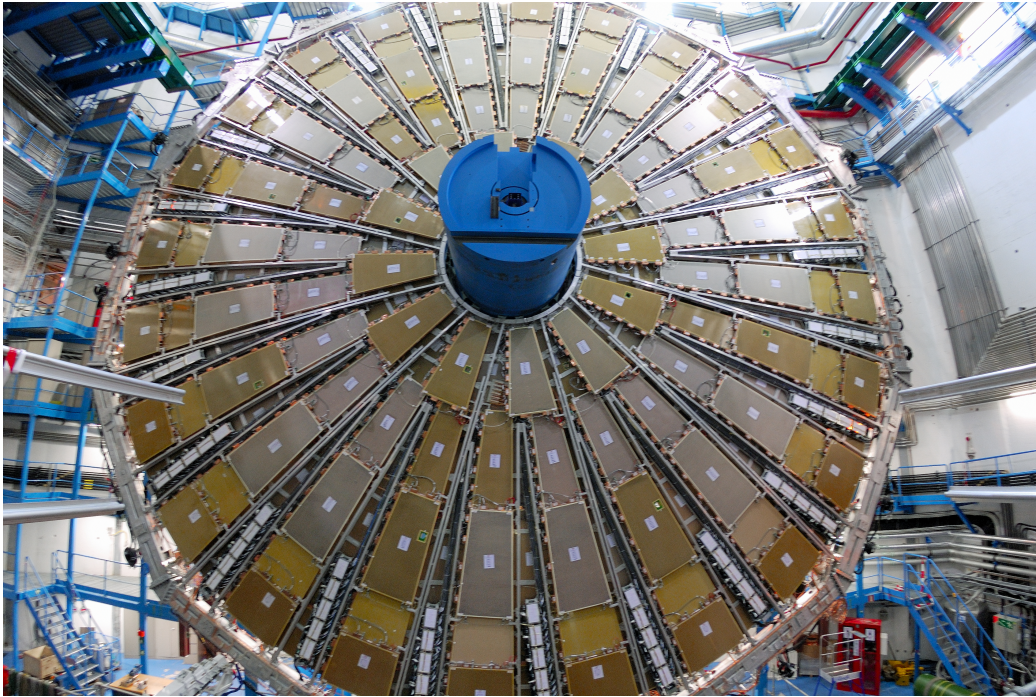
879 a gas mixture of argon and CO₂, which is ionized when muons enter. The detectors
880 operate with a voltage of 1900 V, with much lower drift times than the MDTs. They
881 provide less hits than MDTs, but their lower drift times lower uptime and reduce the
882 amount of detector overload.

883 The CSCs are arranged into four planes on the wheels of the muon spectrometer,
884 as seen in Fig.???. There are 32 CSCs in total, with 16 on each side of the detector
885 in η .

886 **Thin Gap Chambers**

887 The TGCs serve the purpose of the RPCs in the endcap at pseudorapidity of $1.05 <$
888 $|\eta| < 2.4$; they provide fast measurements used in triggering. The TGCs are also
889 multiwire proportional chambers a la the CSCs. The fast readouts necessary for
890 trigger are provided by a high electric field and a small wire-to-wire distance of 1.8
891 mm. These detectors provide both η and ϕ information, allowing the trigger to use
892 as much information as possible when selecting events.

Figure 5.14: Photo of a muon Big Wheel, consisting of Thin Gap Chambers



893 5.5 Trigger System

894 The data rate delivered by the LHC is staggering [89]. In the 2016 dataset, the
895 collision rate was 40 MHz, meaning a *bunch spacing* of 25 ns. In each of the event,
896 as we saw in Ch.??, there are many proton-proton collisions. Most of the collisions
897 are uninteresting, such as elastic scattering of protons, or even inelastic scattering
898 leading to low-energy dijet events. These types of events have been studied in detail
899 in previous experiments.

900 Even if one is genuinely interested in these events, it's *impossible* to save all of
901 the information available in each event. If all events were written "to tape" (as the
902 jargon goes), ATLAS would store terabytes of data per second. We are limited to only
903 about 1000 Hz readout by computing processing time and storage space. We thus
904 implement a *trigger* which provides fast inspection of events to drastically reduce
905 the data rate from the 40 MHz provided by the LHC to the 1000 Hz we can write to
906 tape for further analysis.

907 The ATLAS trigger system consists of a two-level trigger, known as the Level-
908 1 trigger (L1 trigger) and the High-Level Trigger (HLT)⁴. Trigger selections are
909 organized into *trigger chains*, where events passing a particular L1 trigger are passed
910 to a corresponding HLT trigger. For example, one would require a particular high- p_T
911 muon at L1, with additional quality requirements at HLT. One can also use HLT
912 triggers as prerequisites for each other, as is done in some triggers requiring both jets
913 and E_T^{miss} .

914 **Level-1 Trigger**

915 The L1 trigger is hardware-based, and provides the very fast rejection needed to
916 quickly select events of interest. The L1 trigger uses only what is known as *prompt*
917 data to quickly identify interesting events. Only the calorimeters and the triggering
918 detectors (RPCs and TGCs) of the MS are fast enough to be considered at L1,
919 since the tracking reconstruction algorithms used by the ID and the more precise
920 MS detectors are very slow. This allows quick identification of events with the
921 most interesting physical objects : large missing transverse momentum and high-
922 p_T electrons, muons, and jets.

923 L1 trigger processing is done locally. This means that events are selected without
924 considering the entire available event. Energy deposits over some threshold are
925 reconstructed as *regions of interest*. These RoIs are then compared using pattern
926 recognition hardware to “expected” patterns for the given RoIs. Events with RoIs
927 matching these expected patterns are then handed to the HLT through the Central
928 Trigger Processor. This step alone lowers the data rate down by about three orders
929 of magnitude.

⁴In Run1, ATLAS ran with a three-level trigger system. The L1 was essentially as today; the HLT consisted of two separate systems known as the L2 trigger and the Event Filter (EF). This was changed to the simpler system used today during the shutdown between Run1 and Run2.

930 **High-Level Trigger**

931 The HLT performs the next step, taking the incoming data rate from the L1 trigger
932 of ~ 75 kHz down to the ~ 1 kHz that can be written to tape. The HLT really
933 performs much like a simplified offline reconstruction, using many common quality
934 and analysis cuts to eliminate uninteresting events. This is done by using computing
935 farms located close to the detector, which process events in parallel. Individually, each
936 event which enters the computing farms takes about 4 seconds to reconstruct; the
937 HLT reconstruction time also has a long tail, which necessitates careful monitoring
938 of the HLT to ensure smooth operation.

939 HLT triggers are targetted to a particular physics process, such as a E_T^{miss} trigger,
940 single muon trigger, or multijet trigger. The collection of all triggers is known as
941 the trigger *menu*. Since many low-energy particles are produced in collisions, it is
942 necessary to set a *trigger threshold* on the object of interest; this is really just a fancy
943 naming for a trigger p_T cut. Due to the changing luminosity conditions of the LHC,
944 these thresholds change constantly, mostly by increasing thresholds with increasing
945 instantaneous luminosity. This allows an approximately constant number of events to be
946 written for further analysis. Triggers which have rates higher than those designated
947 by the menu are *prescaled*. This means writing only some fraction of the triggered
948 events. Of course, for physics analyses, one wishes to investigate all data events
949 passing some set of analysis cuts, so often one uses the “lowest threshold unprescaled
950 trigger”. *Turn-on curves* allow one to select the needed offline analysis cut to ensure
951 the trigger is fully efficient. An example turn-on curve for the E_T^{miss} triggers used in
952 the signal region of this analysis is shown in ??.

953 The full set of the lowest threshold unprescaled triggers considered here can be
954 found in Table 5.1. These are the lowest unprescaled triggers associated to the SUSY
955 signal models and Standard Model backgrounds considered in this thesis. More
956 information can be found in [89].

Table 5.1: High-Level Triggers used in this thesis. Descriptions of loose, medium, tight, and isolated can be found in [89]. The d_0 cut refers to a quality cut on the vertex position; this was removed from many triggers in 2016 to increase sensitivity to displaced vertex signals. For most triggers, the increased thresholds in 2016 compared to 2015 were designed to keep the rate approximately equal. The exception is the E_T^{miss} triggers; see 5.5.

Physics Object	Trigger	p_T (GeV)	Threshold	Level-1 Seed	Additional Requirements	Approximate Rate (Hz)
2015 Data						
E_T^{miss}	HLT_xe70	70		L1_XE50	-	60
	HLT_mu24_iloose_L1 M145			L1_MU15	isolated, loose	130
Muon	HLT_mu50	50		L1_MU15	-	30
Muon	HLT_e24_1hmedium_l1 B4se_L1EM20VH			L1_EM20VH	medium OR isolated, loose	140
Electron	HLT_e60_1hmedium	60		L1_EM20VH	medium	10
Electron	HLT_e120_1hloose	120		L1_EM20VH	loose	<10
Electron	HLT_g120_loose	120		L1_EM20VH	loose	20
2016 Data						
E_T^{miss}	HLT_xe100_mht_L1 XE500			L1_XE50	-	180
	HLT_mu24_ivarmedium 4			L1_MU20	medium	120
Muon	HLT_mu50	50		L1_MU20	-	40
Muon	HLT_e24_l1tight_no d4ivarloose			L1_EM22VHT	tight with no d_0 or loose	110
Electron	HLT_e60_1hmedium_no d0			L1_EM22VHT	medium with no d_0	10
Electron	HLT_e140_1hloose_no d0			L1_EM22VHT	loose with no d_0	<10
Electron	HLT_g140_loose	140		L1_EM22VHT	loose	20

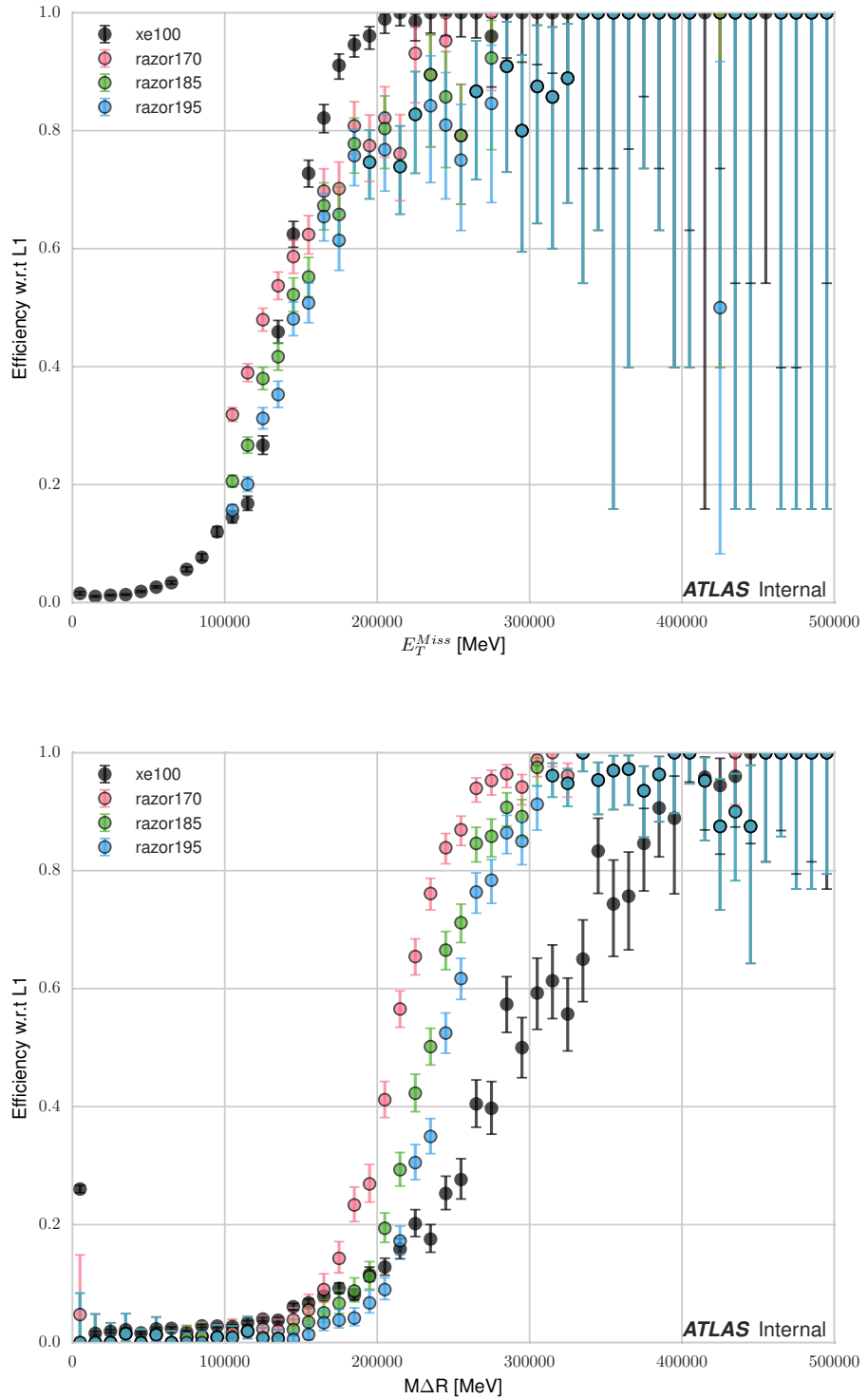
957 **Razor Triggers**

958 For the analysis presented in this thesis, the *razor triggers* were developed. These are
959 topological triggers, combining both jet and E_T^{miss} information to select interesting
960 events. In particular, they use the razor variable M_{Δ}^R which will be described in
961 Chapter ??.

962 Based on 2015 run conditions, these triggers would have allowed the use of a lower
963 offline E_T^{miss} cut with a similar rate to the nominal E_T^{miss} triggers. This can be seen
964 in the turn-on curves shown in Figure 5.15. The razor triggers are fully efficient at
965 nearly 100 GeV lower than the corresponding E_T^{miss} triggers in M_{Δ}^R .

966 There was a quite big change in the 2016 menu, which increased the rate given to
967 E_T^{miss} triggers drastically. This can be seen in the difference in rate shown between
968 E_T^{miss} triggers in 2015 and 2016 in Table 5.1. This allowed the E_T^{miss} triggers to
969 maintain a lower threshold throughout the dataset used in this thesis.

Figure 5.15: Turn-on curves for the razor triggers and nominal E_T^{miss} trigger. The razor triggers show a much sharper turn-on in M_{Δ}^R relative to the E_T^{miss} trigger. The converse is true for the E_T^{miss} triggers.



970

Chapter 6

971

The Large Hadron Collider

972

6.1 Primitive Object Reconstruction

973

Tracks

974

Calorimeter Topoclusters

975

6.2 Physics Object Reconstruction

976

Electrons

977

Photons

978

Muons

979

Jets

980

Missing Transverse Momentum

981

Chapter 7

982

The Recursive Jigsaw Technique

983 Here you can write some introductory remarks about your chapter. I like to give each
984 sentence its own line.

985 When you need a new paragraph, just skip an extra line.

986 **7.1 Razor variables**

987 By using the asterisk to start a new section, I keep the section from appearing in the
988 table of contents. If you want your sections to be numbered and to appear in the
989 table of contents, remove the asterisk.

990 **7.2 SuperRazor variables**

991 **7.3 The Recursive Jigsaw Technique**

992 **7.4 Variables used in the search for zero lepton**

993 **SUSY**

994

Chapter 8

995

Title of Chapter 1

996

Chapter 9

997

Title of Chapter 1

998 Here you can write some introductory remarks about your chapter. I like to give each
999 sentence its own line.

1000 When you need a new paragraph, just skip an extra line.

1001 9.1 Object reconstruction

1002 Photons, Muons, and Electrons

1003 Jets

1004 Missing transverse momentum

1005 Probably longer, show some plots from the PUB note that we worked on

1006 **9.2 Signal regions**

1007 **Gluino signal regions**

1008 **Squark signal regions**

1009 **Compressed signal regions**

1010 **9.3 Background estimation**

1011 **Z vv**

1012 **W ev**

1013 **ttbar**

1014

Chapter 10

1015

Title of Chapter 1

1016 Here you can write some introductory remarks about your chapter. I like to give each
1017 sentence its own line.

1018 When you need a new paragraph, just skip an extra line.

1019 10.1 Statistical Analysis

1020 maybe to be moved to an appendix

1021 10.2 Signal Region distributions

1022 10.3 Pull Plots

1023 10.4 Systematic Uncertainties

1024 10.5 Exclusion plots

1025

Conclusion

1026 Here you can write some introductory remarks about your chapter. I like to give each
1027 sentence its own line.

1028 When you need a new paragraph, just skip an extra line.

1029 **10.6 New Section**

1030 By using the asterisk to start a new section, I keep the section from appearing in the
1031 table of contents. If you want your sections to be numbered and to appear in the
1032 table of contents, remove the asterisk.

Bibliography

- 1034 [1] O. Perdereau, *Planck 2015 cosmological results*,
1035 AIP Conf. Proc. **1743** (2016) p. 050014.
- 1036 [2] N. Aghanim et al.,
1037 *Planck 2016 intermediate results. LI. Features in the cosmic microwave*
1038 *background temperature power spectrum and shifts in cosmological parameters*
1039 (2016), arXiv: [1608.02487 \[astro-ph.CO\]](https://arxiv.org/abs/1608.02487).
- 1040 [3] J. S. Schwinger,
1041 *On Quantum electrodynamics and the magnetic moment of the electron*,
1042 Phys. Rev. **73** (1948) p. 416.
- 1043 [4] S. Laporta and E. Remiddi,
1044 *The Analytical value of the electron (g-2) at order alpha**3 in QED*,
1045 Phys. Lett. **B379** (1996) p. 283, arXiv: [hep-ph/9602417 \[hep-ph\]](https://arxiv.org/abs/hep-ph/9602417).
- 1046 [5] S. Schael et al., *Precision electroweak measurements on the Z resonance*,
1047 Phys. Rept. **427** (2006) p. 257, arXiv: [hep-ex/0509008 \[hep-ex\]](https://arxiv.org/abs/hep-ex/0509008).
- 1048 [6] S. L. Glashow, *Partial Symmetries of Weak Interactions*,
1049 Nucl. Phys. **22** (1961) p. 579.
- 1050 [7] S. Weinberg, *A Model of Leptons*, Phys. Rev. Lett. **19** (1967) p. 1264.
- 1051 [8] A. Salam, *Weak and Electromagnetic Interactions*,
1052 Conf. Proc. **C680519** (1968) p. 367.
- 1053 [9] M. Gell-Mann, *A Schematic Model of Baryons and Mesons*,
1054 Phys. Lett. **8** (1964) p. 214.
- 1055 [10] G. Zweig, “An SU(3) model for strong interaction symmetry and its breaking.
1056 Version 2,” *DEVELOPMENTS IN THE QUARK THEORY OF HADRONS*.
1057 VOL. 1. 1964 - 1978, ed. by D. Lichtenberg and S. P. Rosen, 1964 p. 22,
1058 URL: <http://inspirehep.net/record/4674/files/cern-th-412.pdf>.

- 1059 [11] S. Weinberg, *Implications of Dynamical Symmetry Breaking*,
 1060 Phys. Rev. **D13** (1976) p. 974.
- 1061 [12] S. Weinberg, *Implications of Dynamical Symmetry Breaking: An Addendum*,
 1062 Phys. Rev. **D19** (1979) p. 1277.
- 1063 [13] E. Gildener, *Gauge Symmetry Hierarchies*, Phys. Rev. **D14** (1976) p. 1667.
- 1064 [14] L. Susskind,
 1065 *Dynamics of Spontaneous Symmetry Breaking in the Weinberg-Salam Theory*,
 1066 Phys. Rev. **D20** (1979) p. 2619.
- 1067 [15] S. P. Martin, “A Supersymmetry Primer,” 1997,
 1068 eprint: [arXiv:hep-ph/9709356](https://arxiv.org/abs/hep-ph/9709356).
- 1069 [16] V. C. Rubin and W. K. Ford Jr., *Rotation of the Andromeda Nebula from a*
 1070 *Spectroscopic Survey of Emission Regions*, Astrophys. J. **159** (1970) p. 379.
- 1071 [17] M. S. Roberts and R. N. Whitehurst,
 1072 *“The rotation curve and geometry of M31 at large galactocentric distances*,
 1073 Astrophys. J. **201** (1970) p. 327.
- 1074 [18] V. C. Rubin, N. Thonnard, and W. K. Ford Jr.,
 1075 *Rotational properties of 21 SC galaxies with a large range of luminosities and*
 1076 *radii, from NGC 4605 /R = 4kpc/ to UGC 2885 /R = 122 kpc/*,
 1077 Astrophys. J. **238** (1980) p. 471.
- 1078 [19] V. C. Rubin et al., *Rotation velocities of 16 SA galaxies and a comparison of*
 1079 *Sa, Sb, and SC rotation properties*, Astrophys. J. **289** (1985) p. 81.
- 1080 [20] A. Bosma,
 1081 *21-cm line studies of spiral galaxies. 2. The distribution and kinematics of*
 1082 *neutral hydrogen in spiral galaxies of various morphological types.*,
 1083 Astron. J. **86** (1981) p. 1825.
- 1084 [21] M. Persic, P. Salucci, and F. Stel, *The Universal rotation curve of spiral*
 1085 *galaxies: 1. The Dark matter connection*,
 1086 Mon. Not. Roy. Astron. Soc. **281** (1996) p. 27,
 1087 arXiv: [astro-ph/9506004](https://arxiv.org/abs/astro-ph/9506004) [[astro-ph](#)].
- 1088 [22] M. Lisanti, “Lectures on Dark Matter Physics,” 2016,
 1089 eprint: [arXiv:1603.03797](https://arxiv.org/abs/1603.03797).
- 1090 [23] H. Miyazawa, *Baryon Number Changing Currents*,
 1091 Prog. Theor. Phys. **36** (1966) p. 1266.

- 1092 [24] J.-L. Gervais and B. Sakita, *Generalizations of dual models*,
 1093 Nucl. Phys. **B34** (1971) p. 477.
- 1094 [25] J.-L. Gervais and B. Sakita,
 1095 *Field Theory Interpretation of Supergauges in Dual Models*,
 1096 Nucl. Phys. **B34** (1971) p. 632.
- 1097 [26] Yu. A. Golfand and E. P. Likhtman, *Extension of the Algebra of Poincare
 1098 Group Generators and Violation of p Invariance*,
 1099 JETP Lett. **13** (1971) p. 323, [Pisma Zh. Eksp. Teor. Fiz. 13, 452 (1971)].
- 1100 [27] A. Neveu and J. H. Schwarz, *Factorizable dual model of pions*,
 1101 Nucl. Phys. **B31** (1971) p. 86.
- 1102 [28] A. Neveu and J. H. Schwarz, *Quark Model of Dual Pions*,
 1103 Phys. Rev. **D4** (1971) p. 1109.
- 1104 [29] D. V. Volkov and V. P. Akulov, *Is the Neutrino a Goldstone Particle?*
 1105 Phys. Lett. **B46** (1973) p. 109.
- 1106 [30] J. Wess and B. Zumino,
 1107 *A Lagrangian Model Invariant Under Supergauge Transformations*,
 1108 Phys. Lett. **B49** (1974) p. 52.
- 1109 [31] A. Salam and J. A. Strathdee, *Supersymmetry and Nonabelian Gauges*,
 1110 Phys. Lett. **B51** (1974) p. 353.
- 1111 [32] S. Ferrara, J. Wess, and B. Zumino, *Supergauge Multiplets and Superfields*,
 1112 Phys. Lett. **B51** (1974) p. 239.
- 1113 [33] J. Wess and B. Zumino, *Supergauge Transformations in Four-Dimensions*,
 1114 Nucl. Phys. **B70** (1974) p. 39.
- 1115 [34] J. D. Lykken, “Introduction to supersymmetry,” *Fields, strings and duality. Proceedings, Summer School, Theoretical Advanced Study Institute in Elementary Particle Physics, TASI’96, Boulder, USA, June 2-28, 1996*,
 1116 p. 85, arXiv: [hep-th/9612114 \[hep-th\]](https://arxiv.org/abs/hep-th/9612114),
 1117 URL: http://lss.fnal.gov/cgi-bin/find_paper.pl?pub-96-445-T.
- 1120 [35] A. Kobakhidze, “Intro to SUSY,” 2016, URL:
 1121 <https://indico.cern.ch/event/443176/page/5225-pre-susy-programme>.
- 1122 [36] G. R. Farrar and P. Fayet, *Phenomenology of the Production, Decay, and
 1123 Detection of New Hadronic States Associated with Supersymmetry*,
 1124 Phys. Lett. **B76** (1978) p. 575.

- 1125 [37] ATLAS Collaboration,
 1126 *Search for the electroweak production of supersymmetric particles in*
 1127 *$\sqrt{s} = 8 \text{ TeV}$ pp collisions with the ATLAS detector,*
 1128 *Phys. Rev. D* **93** (2016) p. 052002, arXiv: [1509.07152 \[hep-ex\]](#).
- 1129 [38] ATLAS Collaboration, *Summary of the searches for squarks and gluinos using*
 1130 *$\sqrt{s} = 8 \text{ TeV}$ pp collisions with the ATLAS experiment at the LHC,*
 1131 *JHEP* **10** (2015) p. 054, arXiv: [1507.05525 \[hep-ex\]](#).
- 1132 [39] ATLAS Collaboration, *ATLAS Run 1 searches for direct pair production of*
 1133 *third-generation squarks at the Large Hadron Collider,*
 1134 *Eur. Phys. J. C* **75** (2015) p. 510, arXiv: [1506.08616 \[hep-ex\]](#).
- 1135 [40] CMS Collaboration,
 1136 *Search for supersymmetry with razor variables in pp collisions at $\sqrt{s} = 7 \text{ TeV}$,*
 1137 *Phys. Rev. D* **90** (2014) p. 112001, arXiv: [1405.3961 \[hep-ex\]](#).
- 1138 [41] CMS Collaboration, *Inclusive search for supersymmetry using razor variables*
 1139 *in pp collisions at $\sqrt{s} = 7 \text{ TeV}$, Phys. Rev. Lett.* **111** (2013) p. 081802,
 1140 arXiv: [1212.6961 \[hep-ex\]](#).
- 1141 [42] CMS Collaboration, *Search for Supersymmetry in pp Collisions at 7 TeV in*
 1142 *Events with Jets and Missing Transverse Energy,*
 1143 *Phys. Lett. B* **698** (2011) p. 196, arXiv: [1101.1628 \[hep-ex\]](#).
- 1144 [43] CMS Collaboration, *Search for Supersymmetry at the LHC in Events with*
 1145 *Jets and Missing Transverse Energy, Phys. Rev. Lett.* **107** (2011) p. 221804,
 1146 arXiv: [1109.2352 \[hep-ex\]](#).
- 1147 [44] CMS Collaboration, *Search for supersymmetry in hadronic final states using*
 1148 *M_{T2} in pp collisions at $\sqrt{s} = 7 \text{ TeV}$, JHEP* **10** (2012) p. 018,
 1149 arXiv: [1207.1798 \[hep-ex\]](#).
- 1150 [45] CMS Collaboration, *Searches for supersymmetry using the M_{T2} variable in*
 1151 *hadronic events produced in pp collisions at 8 TeV, JHEP* **05** (2015) p. 078,
 1152 arXiv: [1502.04358 \[hep-ex\]](#).
- 1153 [46] CMS Collaboration, *Search for new physics with the M_{T2} variable in all-jets*
 1154 *final states produced in pp collisions at $\sqrt{s} = 13 \text{ TeV}$ (2016),*
 1155 arXiv: [1603.04053 \[hep-ex\]](#).
- 1156 [47] ATLAS Collaboration, *Multi-channel search for squarks and gluinos in*
 1157 *$\sqrt{s} = 7 \text{ TeV}$ pp collisions with the ATLAS detector at the LHC,*
 1158 *Eur. Phys. J. C* **73** (2013) p. 2362, arXiv: [1212.6149 \[hep-ex\]](#).

- 1159 [48] Y. Grossman, “Introduction to the SM,” 2016, URL: <https://indico.fnal.gov/sessionDisplay.py?sessionId=3&confId=11505#20160811>.
- 1160
- 1161 [49] ()�.
- 1162 [50] P. W. Higgs, *Broken Symmetries and the Masses of Gauge Bosons*,
1163 *Phys. Rev. Lett.* **13** (1964) p. 508.
- 1164 [51] ATLAS Collaboration, *Observation of a new particle in the search for the*
1165 *Standard Model Higgs boson with the ATLAS detector at the LHC*,
1166 *Phys. Lett. B* **716** (2012) p. 1, arXiv: [1207.7214 \[hep-ex\]](https://arxiv.org/abs/1207.7214).
- 1167 [52] CMS Collaboration, *Observation of a new boson at a mass of 125 GeV with*
1168 *the CMS experiment at the LHC*, *Phys. Lett. B* **716** (2012) p. 30,
1169 arXiv: [1207.7235 \[hep-ex\]](https://arxiv.org/abs/1207.7235).
- 1170 [53] A. Chodos et al., *A New Extended Model of Hadrons*,
1171 *Phys. Rev. D* **9** (1974) p. 3471.
- 1172 [54] A. Chodos et al., *Baryon Structure in the Bag Theory*,
1173 *Phys. Rev. D* **10** (1974) p. 2599.
- 1174 [55] J. C. Collins, D. E. Soper, and G. F. Sterman,
1175 *Factorization of Hard Processes in QCD*,
1176 *Adv. Ser. Direct. High Energy Phys.* **5** (1989) p. 1,
1177 arXiv: [hep-ph/0409313 \[hep-ph\]](https://arxiv.org/abs/hep-ph/0409313).
- 1178 [56] K. A. Olive et al., *Review of Particle Physics*,
1179 *Chin. Phys. C* **38** (2014) p. 090001.
- 1180 [57] N. Cabibbo, *Unitary Symmetry and Leptonic Decays*,
1181 *Phys. Rev. Lett.* **10** (1963) p. 531, [,648(1963)].
- 1182 [58] M. Kobayashi and T. Maskawa,
1183 *CP Violation in the Renormalizable Theory of Weak Interaction*,
1184 *Prog. Theor. Phys.* **49** (1973) p. 652.
- 1185 [59] W. F. L. Hollik, *Radiative Corrections in the Standard Model and their Role*
1186 *for Precision Tests of the Electroweak Theory*,
1187 *Fortsch. Phys.* **38** (1990) p. 165.
- 1188 [60] D. Yu. Bardin et al.,
1189 *ELECTROWEAK RADIATIVE CORRECTIONS TO DEEP INELASTIC*
1190 *SCATTERING AT HERA! CHARGED CURRENT SCATTERING*,
1191 *Z. Phys. C* **44** (1989) p. 149.

- 1192 [61] D. C. Kennedy et al., *Electroweak Cross-Sections and Asymmetries at the Z0*,
 1193 Nucl. Phys. **B321** (1989) p. 83.
- 1194 [62] A. Sirlin, *Radiative Corrections in the SU(2)-L x U(1) Theory: A Simple*
 1195 *Renormalization Framework*, Phys. Rev. **D22** (1980) p. 971.
- 1196 [63] S. Fanchiotti, B. A. Kniehl, and A. Sirlin,
 1197 *Incorporation of QCD effects in basic corrections of the electroweak theory*,
 1198 Phys. Rev. **D48** (1993) p. 307, arXiv: [hep-ph/9212285](https://arxiv.org/abs/hep-ph/9212285) [hep-ph].
- 1199 [64] C. Quigg, “Cosmic Neutrinos,” *Proceedings, 35th SLAC Summer Institute on*
 1200 *Particle Physics: Dark matter: From the cosmos to the Laboratory (SSI 2007):*
 1201 *Menlo Park, California, July 30- August 10, 2007*, 2008,
 1202 arXiv: [0802.0013](https://arxiv.org/abs/0802.0013) [hep-ph],
 1203 URL: http://lss.fnal.gov/cgi-bin/find_paper.pl?conf=07-417.
- 1204 [65] S. R. Coleman and J. Mandula, *All Possible Symmetries of the S Matrix*,
 1205 Phys. Rev. **159** (1967) p. 1251.
- 1206 [66] R. Haag, J. T. Lopuszanski, and M. Sohnius,
 1207 *All Possible Generators of Supersymmetries of the s Matrix*,
 1208 Nucl. Phys. **B88** (1975) p. 257.
- 1209 [67] A. Salam and J. A. Strathdee, *On Superfields and Fermi-Bose Symmetry*,
 1210 Phys. Rev. **D11** (1975) p. 1521.
- 1211 [68] S. Dimopoulos and H. Georgi, *Softly Broken Supersymmetry and SU(5)*,
 1212 Nucl. Phys. **B193** (1981) p. 150.
- 1213 [69] S. Dimopoulos, S. Raby, and F. Wilczek,
 1214 *Supersymmetry and the Scale of Unification*, Phys. Rev. **D24** (1981) p. 1681.
- 1215 [70] L. E. Ibanez and G. G. Ross,
 1216 *Low-Energy Predictions in Supersymmetric Grand Unified Theories*,
 1217 Phys. Lett. **B105** (1981) p. 439.
- 1218 [71] W. J. Marciano and G. Senjanovic,
 1219 *Predictions of Supersymmetric Grand Unified Theories*,
 1220 Phys. Rev. **D25** (1982) p. 3092.
- 1221 [72] L. Girardello and M. T. Grisaru, *Soft Breaking of Supersymmetry*,
 1222 Nucl. Phys. **B194** (1982) p. 65.

- 1223 [73] D. J. H. Chung et al.,
 1224 *The Soft supersymmetry breaking Lagrangian: Theory and applications*,
 1225 Phys. Rept. **407** (2005) p. 1, arXiv: [hep-ph/0312378 \[hep-ph\]](#).
- 1226 [74] J. Hisano et al., *Lepton flavor violation in the supersymmetric standard model*
 1227 *with seesaw induced neutrino masses*, Phys. Lett. **B357** (1995) p. 579,
 1228 arXiv: [hep-ph/9501407 \[hep-ph\]](#).
- 1229 [75] F. Gabbiani et al., *A Complete analysis of FCNC and CP constraints in*
 1230 *general SUSY extensions of the standard model*,
 1231 Nucl. Phys. **B477** (1996) p. 321, arXiv: [hep-ph/9604387 \[hep-ph\]](#).
- 1232 [76] F. Gabbiani and A. Masiero, *FCNC in Generalized Supersymmetric Theories*,
 1233 Nucl. Phys. **B322** (1989) p. 235.
- 1234 [77] J. S. Hagelin, S. Kelley, and T. Tanaka, *Supersymmetric flavor changing*
 1235 *neutral currents: Exact amplitudes and phenomenological analysis*,
 1236 Nucl. Phys. **B415** (1994) p. 293.
- 1237 [78] J. S. Hagelin, S. Kelley, and V. Ziegler, *Using gauge coupling unification and*
 1238 *proton decay to test minimal supersymmetric SU(5)*,
 1239 Phys. Lett. **B342** (1995) p. 145, arXiv: [hep-ph/9406366 \[hep-ph\]](#).
- 1240 [79] D. Choudhury et al.,
 1241 *Constraints on nonuniversal soft terms from flavor changing neutral currents*,
 1242 Phys. Lett. **B342** (1995) p. 180, arXiv: [hep-ph/9408275 \[hep-ph\]](#).
- 1243 [80] R. Barbieri and L. J. Hall, *Signals for supersymmetric unification*,
 1244 Phys. Lett. **B338** (1994) p. 212, arXiv: [hep-ph/9408406 \[hep-ph\]](#).
- 1245 [81] B. de Carlos, J. A. Casas, and J. M. Moreno,
 1246 *Constraints on supersymmetric theories from mu —> e gamma*,
 1247 Phys. Rev. **D53** (1996) p. 6398, arXiv: [hep-ph/9507377 \[hep-ph\]](#).
- 1248 [82] J. A. Casas and S. Dimopoulos,
 1249 *Stability bounds on flavor violating trilinear soft terms in the MSSM*,
 1250 Phys. Lett. **B387** (1996) p. 107, arXiv: [hep-ph/9606237 \[hep-ph\]](#).
- 1251 [83] C. Borschensky et al., *Squark and gluino production cross sections in pp*
 1252 *collisions at $\sqrt{s} = 13, 14, 33$ and 100 TeV*, Eur. Phys. J. **C74** (2014) p. 3174,
 1253 arXiv: [1407.5066 \[hep-ph\]](#).
- 1254 [84] M. Klasen, M. Pohl, and G. Sigl, *Indirect and direct search for dark matter*,
 1255 Prog. Part. Nucl. Phys. **85** (2015) p. 1, arXiv: [1507.03800 \[hep-ph\]](#).

- 1256 [85] L. Evans and P. Bryant, *LHC Machine*, JINST **3** (2008) S08001.
- 1257 [86] V. Shiltsev, “Accelerator Physics and Technology,” 2016,
1258 URL: [https://indico.fnal.gov/sessionDisplay.py?sessionId=3&](https://indico.fnal.gov/sessionDisplay.py?sessionId=3&confId=11505#20160811)
1259 [confId=11505#20160811](#).
- 1260 [87] *LEP design report*, Copies shelved as reports in LEP, PS and SPS libraries,
1261 Geneva: CERN, 1984, URL: <https://cds.cern.ch/record/102083>.
- 1262 [88] ATLAS Collaboration,
1263 *The ATLAS Experiment at the CERN Large Hadron Collider*,
1264 JINST **3** (2008) S08003.
- 1265 [89] ATLAS Collaboration, *2015 start-up trigger menu and initial performance*
1266 *assessment of the ATLAS trigger using Run-2 data*,
1267 ATL-DAQ-PUB-2016-001, 2016,
1268 URL: <https://cds.cern.ch/record/2136007/>.

1269

The Standard Model

1270 In this appendix, we provide a brief overview of the basic ingredients involved in
1271 construction of the Standard Model Lagrangian : quantum field theory, symmetries,
1272 and symmetry breaking.

1273 Quantum Field Theory

1274

1275 In this section, we provide a brief overview of the necessary concepts from
1276 Quantum Field Theory (QFT).

cite Yuval's
lectures
and notes
somehow

1277 In modern physics, the laws of nature are described by the “action” S , with the
1278 imposition of the principle of minimum action. The action is the integral over the cite
1279 spacetime coordinates of the “Lagrangian density” \mathcal{L} , or Lagrangian for short. The
1280 Lagrangian is a function of “fields”; general fields will be called $\phi(x^\mu)$, where the
1281 indices μ run over the space-time coordinates. We can then write the action S as

$$S = \int d^4x \mathcal{L}[\phi_i(x^\mu), \partial_\mu \phi_i(x^\mu)] \quad (10.1)$$

1282 where we have an additional summation over i (of the different fields). Generally,
1283 we impose the following constraints on the Lagrangian :

- 1284 1. Translational invariance - The Lagrangian is only a function of the fields ϕ and
1285 their derivatives $\partial_\mu \phi$
- 1286 2. Locality - The Lagrangian is only a function of one point x_μ in spacetime.

- 1287 3. Reality condition - The Lagrangian is real to conserve probability.
- 1288 4. Lorentz invariance - The Lagrangian is invariant under the Poincarégroup of
1289 spacetime.
- 1290 5. Analyticity - The Lagrangian is an analytical function of the fields; this is to
1291 allow the use of perturbation theory.
- 1292 6. Invariance and Naturalness - The Lagrangian is invariant under some internal
1293 symmetry groups; in fact, the Lagrangian will have *all* terms allowed by the
imposed symmetry groups.
- 1294 maybe add
in ref here
- 1295 7. Renormalizability - The Lagrangian will be renormalizable - in practice, this
1296 means there will not be terms with more than power 4 in the fields.

1297 The key item from the point of view of this thesis is that of “Invariance and
1298 Natural”. We impose a set of “symmetries” and then our Lagrangian is the most
1299 general which is allowed by those symmetries.

1300 Symmetries

1301 Symmetries can be seen as the fundamental guiding concept of modern physics.
1302 cite? Symmetries are described by “groups”. To illustrate the importance of symmetries
1303 and their mathematical description, groups, we start here with two of the simplest
1304 and most useful examples : \mathbb{Z}_2 and $U(1)$.

1305 \mathbb{Z}_2 symmetry

1306 \mathbb{Z}_2 symmetry is the simplest example of a “discrete” symmetry. Consider the most
1307 general Lagrangian of a single real scalar field $\phi(x_\mu)$

$$\mathcal{L}_\phi = \frac{1}{2}\partial_\mu\phi\partial^\mu\phi - \frac{m^2}{2}\phi^2 - \frac{\mu}{2\sqrt{2}}\phi^3 - \lambda\phi^4 \quad (10.2)$$

Now we *impose* the symmetry

$$\mathcal{L}(\phi) = \mathcal{L}(-\phi) \quad (10.3)$$

1308 This has the effect of restricting the allowed terms of the Lagrangian. In particular,
 1309 we can see the term $\phi^3 \rightarrow -\phi^3$ under the symmetry transformation, and thus must
 1310 be disallowed by this symmetry. This means under the imposition of this particular
 1311 symmetry, our Lagrangian should be rewritten as

$$\mathcal{L}_\phi = \frac{1}{2}\partial_\mu\phi\partial^\mu\phi - \frac{m^2}{2}\phi^2 - \lambda\phi^4 \quad (10.4)$$

1312 The effect of this symmetry is that the total number of ϕ particles can only change
 1313 by even numbers, since the only interaction term $\lambda\phi^4$ is an even power of the field.
 1314 This symmetry is often imposed in supersymmetric theories, as we will see in Chapter
 1315 3.

1316 **$U(1)$ symmetry**

1317 $U(1)$ is the simplest example of a continuous (or *Lie*) group. Now consider a theory
 1318 with a single complex scalar field $\phi = \text{Re } \phi + i \text{Im } \phi$

$$\mathcal{L}_\phi = \delta_{i,j} \frac{1}{2}\partial_\mu\phi_i\partial^\mu\phi_j - \frac{m^2}{2}\phi_i\phi_j - \frac{\mu}{2\sqrt{2}}\phi_i\phi_j\phi_k\phi_l - \lambda\phi_i\phi_j\phi_k\phi_l \quad (10.5)$$

1319 where $i, j, k, l = \text{Re}, \text{Im}$. In this case, we impose the following $U(1)$ symmetry
 1320 : $\phi \rightarrow e^{i\theta}, \phi^* \rightarrow e^{-i\theta}$. We see immediately that this again disallows the third-order
 1321 terms, and we can write a theory of a complex scalar field with $U(1)$ symmetry as

$$\mathcal{L}_\phi = \partial_\mu\phi\partial^\mu\phi^* - \frac{m^2}{2}\phi\phi^* - \lambda(\phi\phi^*)^2 \quad (10.6)$$

1322 **Local symmetries**

1323 The two examples considered above are “global” symmetries in the sense that the
1324 symmetry transformation does not depend on the spacetime coordinate x_μ . We know
1325 to look at local symmetries; in this case, for example with a local $U(1)$ symmetry, the
1326 transformation has the form $\phi(x_\mu) \rightarrow e^{i\theta(x_\mu)}\phi(x_\mu)$. These symmetries are also known
1327 as “gauge” symmetries; all symmetries of the Standard Model are gauge symmetries.

There are wide-ranging consequences to the imposition of local symmetries. To begin, we note that the derivative terms of the Lagrangian 10.2 are *not* invariant under a local symmetry transformation

$$\partial_\mu \phi(x_\mu) \rightarrow \partial_\mu(e^{i\theta(x_\mu)}\phi(x_\mu)) = (1 + i\theta(x_\mu))e^{i\theta(x_\mu)}\phi(x_\mu) \quad (10.7)$$

GET THIS
RIGHT 1328
1329

This leads us to note that the kinetic terms of the Lagrangian are also not invariant under a gauge symmetry. This would lead to a model with no dynamics, which is clearly unsatisfactory.

1332 Let us take inspiration from the case of global symmetries. We need to define a
1333 so-called “covariant” derivative D^μ such that

$$D^\mu \phi \rightarrow e^{iq\theta(x^\mu)D^\mu}\phi \quad (10.8)$$

$$D^\mu \phi^* \rightarrow e^{-iq\theta(x^\mu)D^\mu}\phi^* \quad (10.9)$$

$$(10.10)$$

1334 Since ϕ and ϕ^* transforms with the opposite phase, this will lead the invariance
1335 of the Lagrangian under our local gauge transformation. This D^μ is of the following
1336 form

$$D^\mu = \partial_\mu - igqA^\mu \quad (10.11)$$

1337 where A^μ is a vector field we introduce with the transformation law

$$A^\mu \rightarrow A^\mu - \frac{1}{g} \partial_\mu \theta \quad (10.12)$$

1338 and g is the coupling constant associated to vector field. This vector field A^μ is
1339 also known as a “gauge” field.

1340 Since we need to add all allowed terms to the Lagrangian, we define

$$F^{\mu\nu} = A^\mu A^\nu - A^\nu A^\mu \quad (10.13)$$

1341 and then we must also add the kinetic term :

$$\mathcal{L}_{\text{gauge}} = -\frac{1}{4} F^{\mu\nu} F_{\mu\nu} \quad (10.14)$$

1342 The most general renormalizable Lagrangian with fermion and scalar fields can
1343 be written in the following form

$$\mathcal{L} = \mathcal{L}_{\text{kin}} + \mathcal{L}_\phi + \mathcal{L}_\psi + \mathcal{L}_{\text{Yukawa}} \quad (10.15)$$

1344 Symmetry breaking and the Higgs mechanism

1345 Here we view some examples of symmetry breaking. We investigate breaking of a
1346 global $U(1)$ symmetry and a local $U(1)$ symmetry. The SM will break the electroweak
1347 symmetry $SU(2)xU(1)$, and in Chapter 3 we will see how supersymmetry must also
1348 be broken.

1349 There are two ideas of symmetry breaking

- 1350 • Explicit symmetry breaking by a small parameter - in this case, we have a small
1351 parameter which breaks an “approximate” symmetry of our Lagrangian. An
1352 example would be the theory of the single scalar field 10.2, when $\mu \ll m^2$ and

1353 $\mu \ll \lambda$. In this case, we can often ignore the small term when considering
 1354 low-energy processes.

1355 • Spontaneous symmetry breaking (SSB) - spontaneous symmetry breaking
 1356 occurs when the Lagrangian is symmetric with respect to a given symmetry
 1357 transformation, but the ground state of the theory is *not* symmetric with respect
 1358 to that transformation. This can have some fascinating consequences, as we
 1359 will see in the following examples

1360 Symmetry breaking a

1361 **U(1) global symmetry breaking**

Consider the theory of a complex scalar field under the $U(1)$ symmetry, or the transformation

$$\phi \rightarrow e^{i\theta} \phi \quad (10.16)$$

The Lagrangian for this theory is

$$\mathcal{L} = \partial^\mu \phi^\dagger \partial_\mu \phi + \frac{\mu^2}{2} \phi^\dagger \phi + \frac{\lambda}{4} (\phi^\dagger \phi)^2 \quad (10.17)$$

Let us write this theory in terms of two scalar fields, h and ξ : $\phi = (h + i\xi)/\sqrt{2}$.

The Lagrangian can then be written as

$$\mathcal{L} = \partial^\mu h \partial_\mu h + \partial^\mu \xi d\mu \xi - \frac{\mu^2}{2} (h^2 + \xi^2) - \frac{\lambda}{4} (h^2 + \xi^2)^2 \quad (10.18)$$

First, note that the theory is only stable when $\lambda > 0$. To understand the effect of SSB, we now enforce that $\mu^2 < 0$, and define $v^2 = -\mu^2/\lambda$. We can then write the scalar potential of this theory as :

$$V(\phi) = \lambda(\phi^\dagger \phi - v^2/2)^2 \quad (10.19)$$

Minimizing this equation with respect to ϕ , we can see that the “vacuum expectation value” of the theory is

$$2 < \phi^\dagger \phi > = < h^2 + \xi^2 > = v^2 \quad (10.20)$$

1362 We now reach the “breaking” point of this procedure. In the (h, ξ) plane, the
 1363 minima form a circle of radius v . We are free to choose any of these minima to expand
 1364 our Lagrangian around; the physics is not affected by this choice. For convenience,
 1365 choose $\langle h \rangle = v, \langle \xi^2 \rangle = 0$.

Now, let us define $h' = h - v, \xi' = \xi$ with VEVs $\langle h' \rangle = 0, \langle \xi' \rangle = 0$. We can
 then write our spontaneously broken Lagrangian in the form

$$\mathcal{L} = \frac{1}{2}\partial_\mu h'\partial^\mu h' + \frac{1}{2}\partial_\mu \xi'\partial^\mu \xi' - \lambda v^2 h'^2 - \lambda v h'(h'^2 + \xi'^2) - \lambda(h'^2 + \xi'^2)^2 \quad (10.21)$$